In presenting the dissertation as a partial fulfillment of the requirements for an advanced degree from the Georgia Institute of Technology, I agree that the Library of the Institute shall make it available for inspection and circulation in accordance with its regulations governing materials of this type. I agree that permission to copy from, or to publish from, this dissertation may be granted by the professor under whose direction it was written, or, in his absence, by the Dean of the Graduate Division when such copying or publication is solely for scholarly purposes and does not involve potential financial gain. It is understood that any copying from, or publication of, this dissertation which involves potential financial gain will not be allowed without written permission.

7/25/68

A MÖSSBAUER INVESTIGATION OF ATOMIC ORDERING

EFFECTS IN THE IRON-COBALT ALLOY SYSTEM

A THESIS

Presented to

The Faculty of the Graduate Division

by

Benjamin deMayo

In Partial Fulfillment

of the Requirements for the Degree

Doctor of Philosophy in the School of Physics
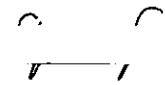

Georgia Institute of Technology
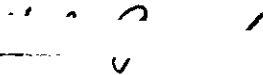
September 1969

A MÖSSBAUER INVESTIGATION OF ATOMIC ORDERING

EFFECTS IN THE IRON-COBALT ALLOY SYSTEM

Approved:

Chairman

Date approved by Chairman: _12 September 1969_

ACKNOWLEDGMENTS

The author wishes to express his sincere appreciation to Dr. D. W. Forester for his guidance and assistance in this investigation. Also, the author wishes to thank Dr. H. A. Gersch, Dr. S. Spooner, Dr. E. A. Starke, and Professor P. A. Beck for many enlightening discussions.

The author is indebted to the National Aeronautics and Space Administration for financial support of this research, and to Dr. S. Spooner for the neutron diffraction results. In addition, N. C. Koon designed and constructed the electronic feedback circuit and developed the data analysis computer program. The author is grateful to Mrs. Gail G. Williams for typing the final draft of this thesis.

The author also wishes to acknowledge the financial support and encouragement of his parents, Mr. and Mrs. Maurice deMayo, during the course of his graduate career.

TABLE OF CONTENTS

TABLE OF CONTENTS (Continued)

LIST OF TABLES

LIST OF ILLUSTRATIONS

LIST OF ILLUSTRATIONS (Continued)

SUMMARY

A knowledge of the relationships between local atomic configurations and magnetic or structural properties of transition metal alloys is of considerable fundamental and technical importance. These relationships are reflected in the dependence on configuration of nuclear hyperfine interactions, which may be studied using the extremely high resolution technique of Mössbauer spectroscopy.

In this study, Mössbauer spectroscopy was applied to the iron-cobalt alloy system, and the atomic configurations were changed by varying the composition and degree of order. Composition dependent studies were made between 25 and 75 atomic percent cobalt, and a detailed study as a function of atomic order was made on the equiatomic alloy Fe(50-50)Co. The effective magnetic field at the iron nuclei, the isomer shift, the quadrupole splitting, and the shapes of the absorption lines of the spectra were measured for the alloy samples. It was found that in this composition region: (1) the effective field and isomer shift are reduced in magnitude with increasing order or with increasing cobalt concentration, (2) the quadrupole splitting is unaffected by ordering or by composition changes, and (3) disordering broadens the absorption lines and ordering narrows them. The results indicate that local atomic configurations play a significant role in the competition between various contributions to the hyperfine interactions. The data imply a positive local spin polarization contribution. Also, the temperature dependence of the short range

order was determined within the framework of a statistical description

of the ordering process.

CHAPTER I

INTRODUCTION

The magnetic, mechanical, and electronic properties of the iron-group transition metals and their alloys with each other have long held the attention of physicists, metallurgists, and engineers. In alloys of iron-cobalt, for example, the combination of a high magnetic moment and unusual structural qualities has led to wide technological application of these alloys and to experimental and theoretical interest in their properties. A thorough knowledge of the physical phenomena which occur in iron-cobalt is important to effective practical utilization and to understanding the basic mechanisms governing the phenomena. Mössbauer spectroscopy, a very versatile research tool of high precision, can be used to study the iron-cobalt alloy system.

The Mössbauer effect, or resonant absorption or emission of gamma rays by nuclei in solids, is the basis of Mössbauer spectroscopy. This method of spectroscopy has been used to study numerous aspects of solid state physics, relativity, and nuclear physics. Such parameters as the effective magnetic field, the electronic charge density, and the electric field gradient can be measured at the nuclei of solids. From these, information is obtained about the electronic wave functions, atomic magnetic moments, and lattice properties, for example.

Of the 45 nuclides which are known to exhibit the Mössbauer

effect, ^{57}Fe is the most widely used in Mössbauer spectroscopy for three main reasons. First, an appreciable amount of resonant absorption is observed in iron at room temperature, obviating the need for complicated refrigeration procedures. Second, iron is a very common element, and ^{57}Fe comprises two percent of naturally occurring iron. Also, iron makes up over five percent of the earth's crust and alloys with 75 percent of all elements. Third, iron is one of the few materials which exhibit ferromagnetism, and in many cases the resulting internal effective magnetic field, which is very large, can be used to observe effects which require fields beyond the current capability of laboratory production.

The Iron-Cobalt Alloy System: Previous Investigations

Iron and cobalt, which lie next to each other in the center of the 3d transition metal series of the periodic table, are both magnetic and form solid solutions with each other over the entire composition range. Figure 1 shows an approximate phase diagram of this alloy system. One of the main features evident is the relatively high melting curve at around 1500 °C. Also, there is a face-centered cubic (fcc) solid solution region down to around 900 °C with a body-centered cubic (bcc) solid solution occurring for temperatures less than 900 °C and compositions less than 75 percent cobalt.[*] The magnetic transition varies with composition and structure between 775 °C and 1100 °C, and

---

[*]All compositions are given in atomic percentages.
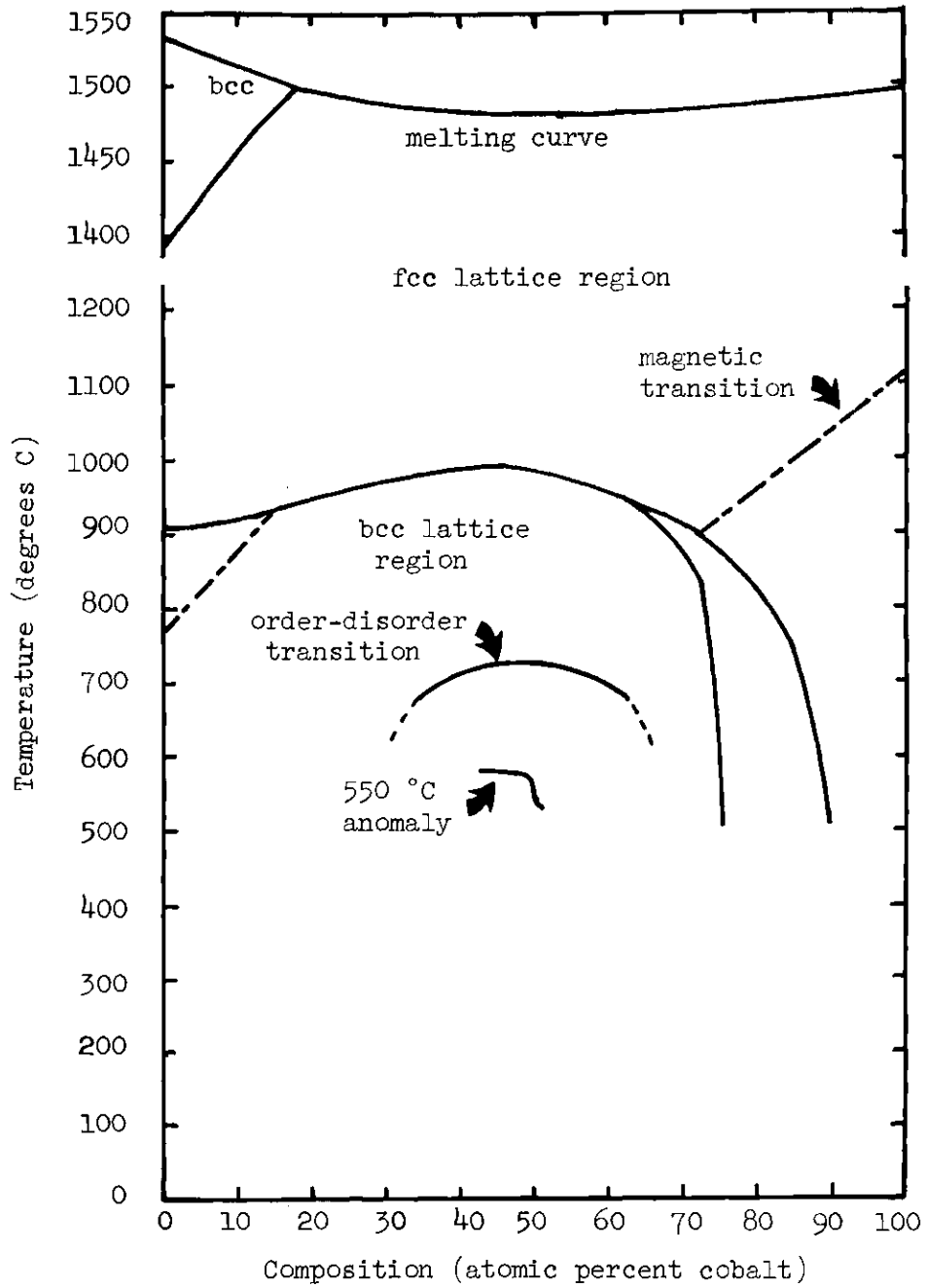
Figure 1. Phase Diagram for the Iron-Cobalt Alloy System (1).

there is an atomic configurational order-disorder transition in the
region of 730 °C and 25 to 75 percent cobalt with the maximum transition
temperature (730 °C) occurring for the equiatomic composition. There
is also evidence of a lower temperature transition, often referred to
as the "550 °C anomaly." This phase diagram was constructed from the
results of x-ray and neutron diffraction, magnetization, resistivity,
specific heat, thermo-electromotive force, thermal expansion, and
thermal conductivity experiments (1). Information about atomic order-
disorder phenomena in this system comes primarily from specific heat
and neutron diffraction measurements; x-ray measurements are of little
assistance since iron and cobalt have almost identical x-ray scattering
factors.

It has been found that this alloy system possesses the highest
magnetic moment per atom of all of the 3d transition-metal alloys.
This is shown in the "Slater-Pauling curve" (2,3,4) which is given in
Figure 2, a plot of the magnetic moment per atom for the transition
metal alloys as a function of the number of (3d + 4s) electrons per
atom for each alloy. The fact that iron-cobalt lies at the peak of
this curve indicates one reason why this system has been so extensively
studied. The peak occurs at around 30 percent cobalt and with a magnetic
moment per atom value of 2.5 μ_B, where μ_B is the Bohr magneton,
0.927 x 10^{-20} erg/oersted.

Recently bulk magnetization studies have been used to determine
the average magnetic moment per atom for iron-cobalt alloy samples both
in the ordered and disordered states (5). These results are given in
Figure 3, which shows that between 25 and 75 percent cobalt the average
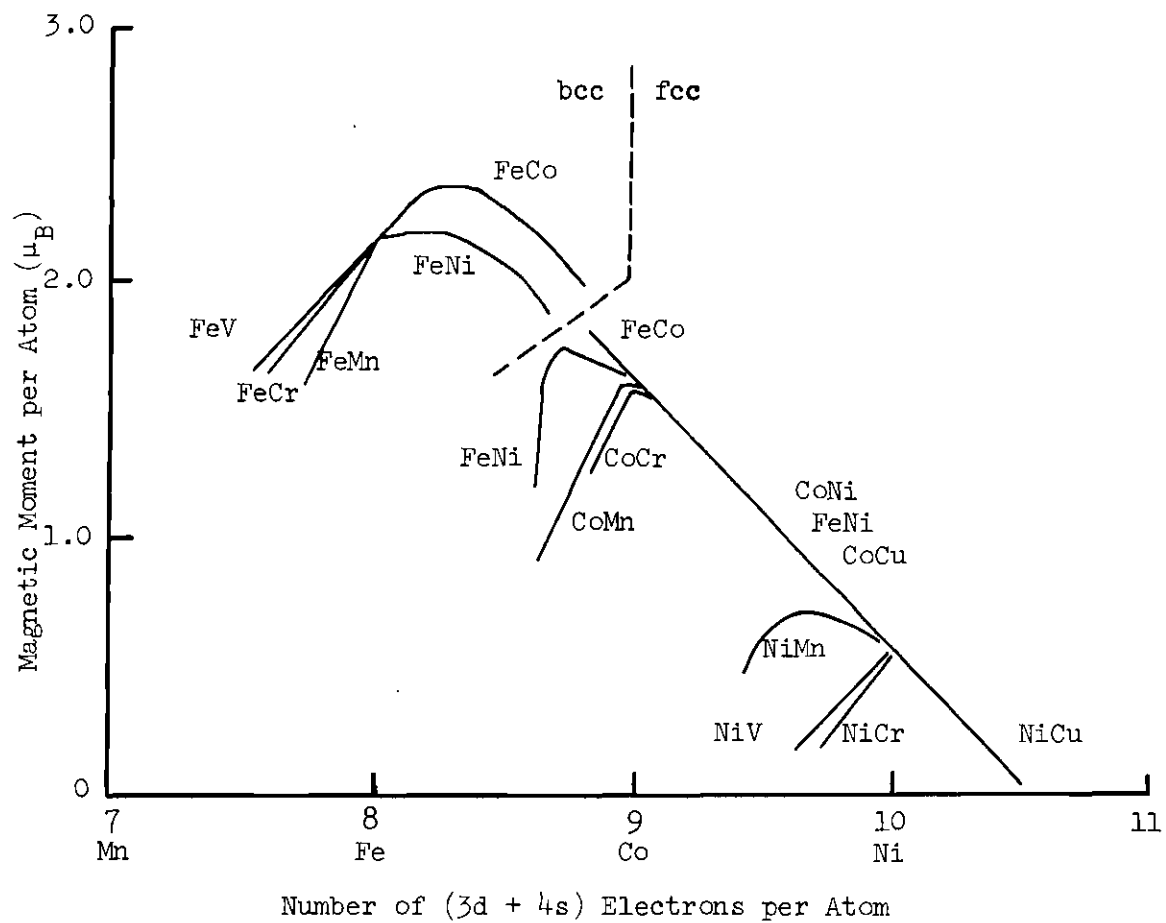
Figure 2. Average Magnetic Moment per Atom versus the Number of (3d + 4s) Electrons per Atom (4).
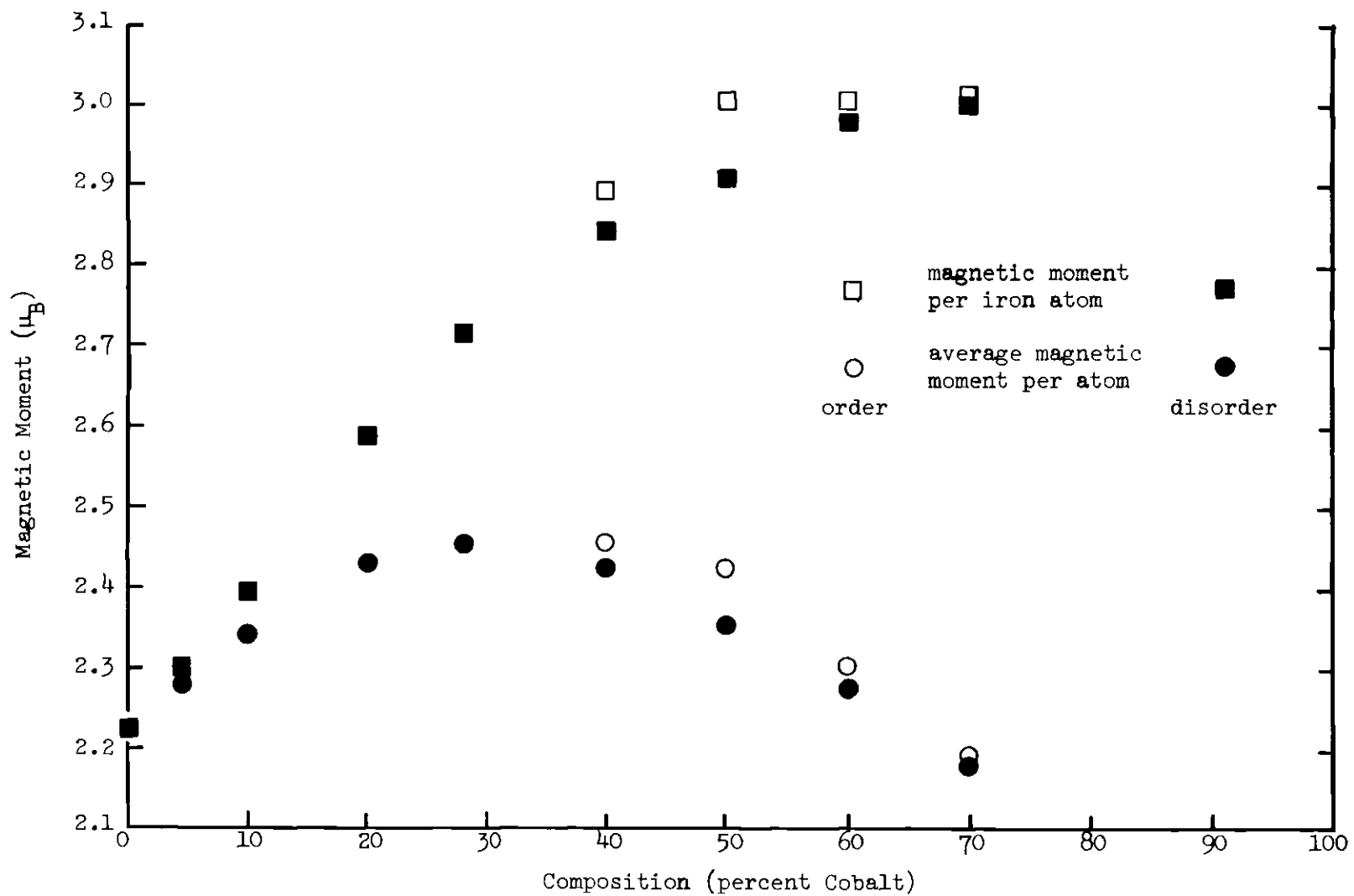
Figure 3. Average Magnetic Moment per Atom and Magnetic Moment per Iron Atom (Assuming a Constant Cobalt Magnetic Moment) versus Composition for Iron-Cobalt (5).

magnetic moment per atom is larger for the ordered samples than for

disordered samples of the same composition. The maximum difference

in moment between ordered and disordered samples is three percent at

50 percent cobalt. Also shown in Figure 3 is the average moment per

iron atom. Neutron diffraction measurements can determine the local

moment on the constituent atoms of an alloy. Such measurements on

iron-cobalt suggest that the cobalt moment is not affected by

alloying and remains at approximately 1.8 μ_B over the entire composition

range (6,7). On the other hand, the iron moment increases with increasing

cobalt concentration from 2.2 μ_B in pure iron to about 3.0 μ_B at

around 40-50 percent cobalt and remains constant with the addition

of more cobalt. If the value obtained for the cobalt moment is

combined with the magnetization data, then the dependence of the iron

moment on atomic order as well as composition may be calculated, as

shown in Figure 3. The results infer that the iron moment is increased

by as much as three percent by ordering.

The lattice parameter of iron-cobalt has been measured as a

function of composition and order (8,9) as shown in Figure 4. This

parameter remains constant with increasing cobalt concentration to

about 20 percent cobalt and then decreases linearly by about nine

percent at 70 percent cobalt. The dependence of the lattice parameter

on order is complicated and small.

The low temperature electronic specific heat coefficient of

iron-cobalt has been found to have a pronounced minimum at around

30 percent cobalt (10), which implies that the average density of

states at the Fermi surface is a minimum at this composition (11,12).
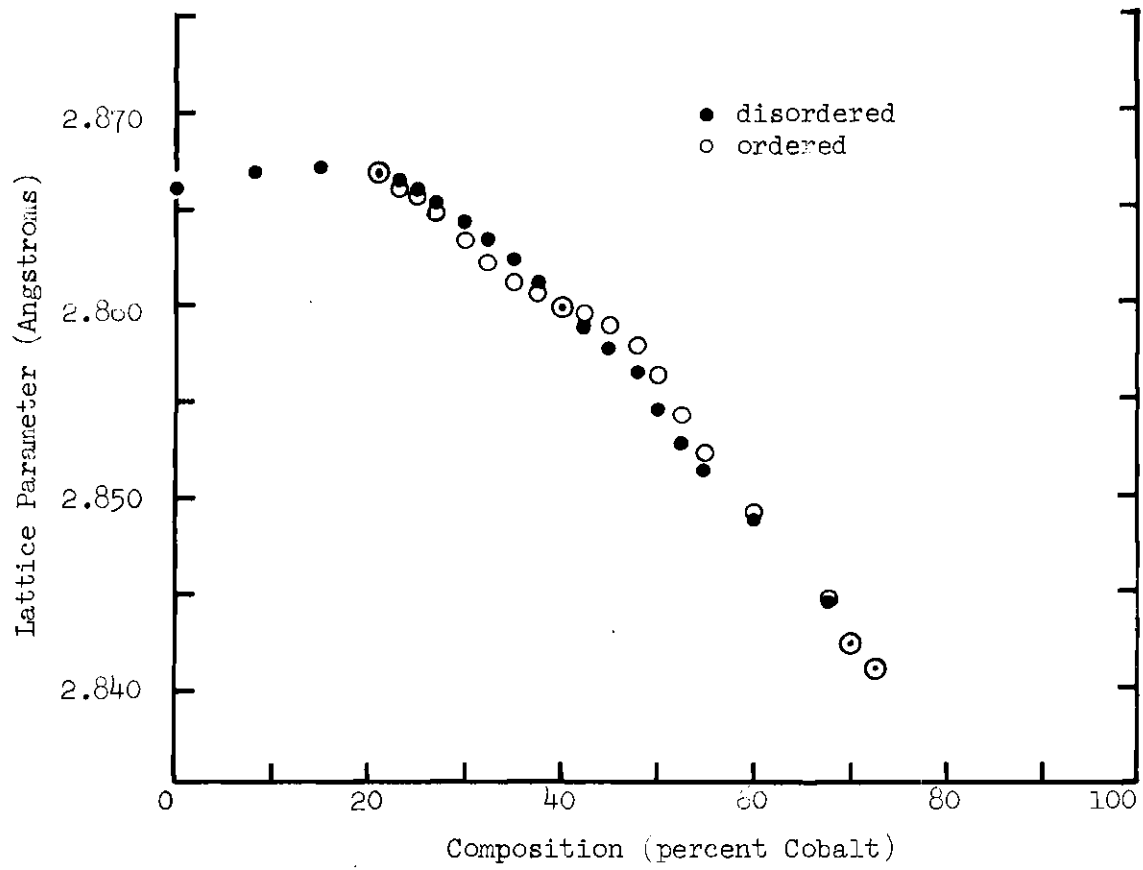
Figure 4. Lattice Parameter of Iron-Cobalt versus Composition (8).

The effective magnetic field at the iron nuclei, H_e, has been measured in iron-cobalt alloys using the techniques of Mössbauer spectroscopy and nuclear magnetic resonance (NMR). In dilute cobalt-in-iron alloys, the results have been interpreted in terms of the contributions to the effective field of an iron atom by its cobalt near neighbors. Wertheim et al. (13) using Mössbauer spectroscopy determined that each cobalt first and second neighbor to an iron atom increased the magnitude of H_e by 14.7 kOe and 7.1 kOe, respectively. Rubenstein (14) used NMR to study these dilute alloys and found that the first and second cobalt neighbor contributions also increased the magnitude of H_e but only by 4.7 kOe for both of the neighbor types. The effective field in pure iron has been measured, using Mössbauer spectroscopy and NMR, to be -330 kOe at room temperature, the negative sign indicating that its direction is opposite to that of the internal magnetization (15,16,17). Thus the effects of local environment on H_e are seen to be relatively small, but there is disagreement concerning their actual magnitudes.

The Mössbauer measurements of H_e have been extended over the entire composition range of the iron-cobalt system by Johnson et al. (18,19,20). They reported a peak in the magnitude of H_e of about 365 kOe at 30 percent cobalt. Although these authors did not attempt to gain information about the local contributions to H_e from cobalt neighbors to the iron atoms, they did point out that H_e is not strictly proportional to the local magnetic moment of the iron atoms. In a conference report (19), they cite an effect of atomic order on H_e, with the effective field being larger in magnitude for ordered

samples than for disordered samples. However, there was no extensive study made of this apparent effect and their final publication (20) makes no mention of it. Furthermore, they refer to no independent method, such as neutron diffraction, for determining the state of order in their samples. There have been no NMR studies reported on concentrated iron-cobalt alloys.

The purpose of this research was to use Mössbauer spectroscopy to study the 25 to 75 percent composition range of the iron-cobalt alloy system, with particular attention being paid to the state of atomic order in the samples. From the previous discussion, it can be seen that the Mössbauer investigations of H_e for iron-cobalt in this composition region are incomplete. In addition there are no detailed results available on the isomer shift, the quadrupole splitting, or line broadening effects in this composition region, although these results are expected to yield information concerning the contributions to H_e. Preliminary results of this research have already been reported (21).

Atomic Order and Disorder

Atomic configurational order-disorder phenomena in alloys affect such physical properties as the local atomic magnetic moments and the mechanical qualities of the alloys. Detailed reviews (22,23,24,25) discuss these phenomena; in the present section, some aspects of order-disorder pertinent to the iron-cobalt alloy system are given.

As early as 1934, Bragg and Williams (26,27) formulated a theory

of atomic order in binary alloys to explain the dependence of the specific heat of the alloys on their previous thermal and mechanical treatments. They introduced a parameter S to be a measure of the amount of long range atomic order present in an alloy. S has a magnitude of unity for low temperatures and decreases to zero at a critical temperature, T_c, as the temperature is raised. Figure 5 shows this temperature dependence for a typical binary alloy (17). To see the physical significance of the long range order parameter S, consider a binary alloy of atom-types A and B in equal concentration and of a bcc lattice structure. When the alloy is completely ordered, the A-atoms may be thought of as occupying one simple cubic lattice "a," and the B-atoms may similarly be thought of as occupying another, interpenetrating simple cubic lattice, called "b." S is equal to unity for this case. For complete disorder, each lattice site has a 50 percent probability of being occupied by either type of atom. S is zero for this case. Figure 6 shows the atomic configurations in the two extreme cases of complete order and complete disorder. In the Bragg-Williams formulation, for intermediate degrees of order, S is related to the number of A-atoms on the "a" type lattice sites and to the number of B-atoms on the "b" lattice sites. In this way, S is a measure of the degree of configurational atomic order in the entire lattice.

Bethe (28) pointed out that there could also exist atomic short range order in the lattice. This behavior was later characterized by Cowley (27) using a set of parameters α_i, each parameter α_i being defined as the short range order parameter of the ith neighbor shell
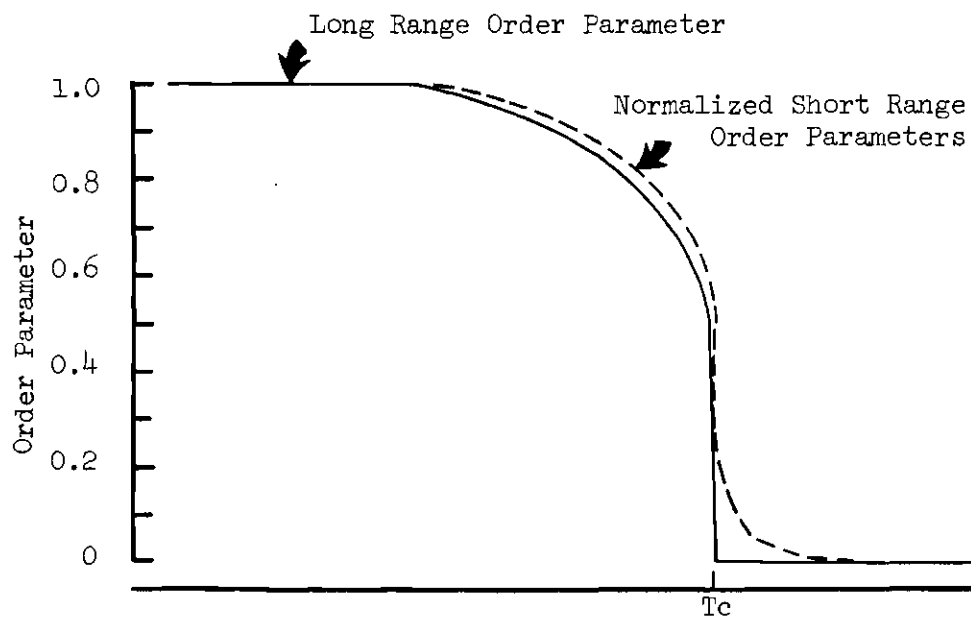
Figure 5. Long Range Order Parameter and Normalized Short Range Order
Parameters for a Typical Binary Alloy versus Temperature
(27). (Tc is the order-disorder transition temperature.
For purposes of illustration, the short range order
parameters are assumed to have the same temperature
dependence.)
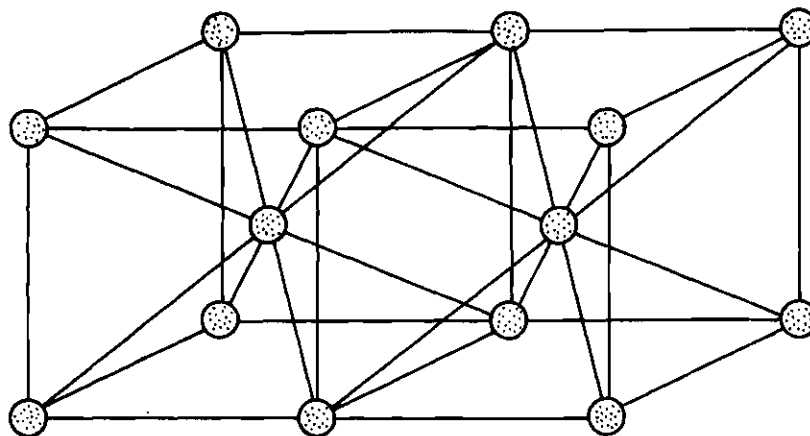
a) Disordered Fe(50-50)Co. ⊛ indicates equal chance of atom being iron or cobalt.
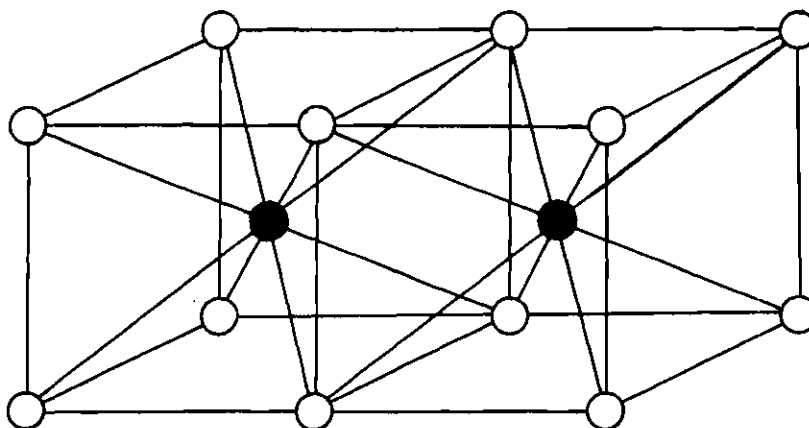
b) Ordered Fe(50-50)Co. ● indicates an iron atom.

○ indicates a cobalt atom.

Figure 6. Disordered and Ordered Fe(50-50)Co.

of a particular atom in the lattice. All of the α_i's are zero for complete disorder, and they have different non-zero values for complete order which depend on the lattice type, the composition, and the neighbor shell. The α_i's can be normalized to equal unity for complete order.

The two types of order parameters are related; their relative temperature dependence is shown in Figure 5. The absolute magnitude of the normalized short range order parameters does not go to zero at T_c; instead, it decreases gradually as the temperature is raised above T_c.

By changing the amount of order in an alloy sample, the local atomic environments of the individual atoms can be changed without changing the composition. For example, in disordered Fe(50-50)Co, each iron atom has four cobalt nearest neighbors, on the average. On the other hand, when the alloy is ordered, each iron atom has eight cobalt nearest neighbors.

Mössbauer Spectroscopy

The Mössbauer effect (29) occurs when gamma ray emission or absorption by a nucleus imbedded in a solid is not accompanied by an excitation of phonons. That is, the nucleus recoils only as a part of a larger, rigid assembly of atoms. In this case, the gamma ray can be resonantly re-absorbed or re-emitted since it suffers negligible energy loss due to the recoil. In iron at room temperature, over 85 percent of the ^{57}Fe 14.4 keV gamma ray transitions are of this type. The natural line width of these Mössbauer transitions is about

5×10^{-9} eV, providing a possible resolution of about one part in 10^{12}. Since the experimentally realized resolution is very close to this, it can be seen that Mössbauer spectroscopy is potentially a very precise research tool.

The basic aspects for experimentally observing Mössbauer spectra are illustrated in Figure 7. A velocity transducer gives to the gamma rays emitted by a radioactive source a Doppler energy, which may be scanned by varying the velocity of the source. Ordinarily the gamma rays pass through the absorber without being resonantly absorbed (Figure 7b). When the velocity of the source is just that necessary for the gamma rays to be resonantly absorbed by the Mössbauer nuclei in the absorber, the detector measures a drop in the intensity of gamma rays reaching it (Figure 7c). Although the gamma rays are incident on the absorber from one direction, when resonant absorption occurs the gamma rays will be re-emitted in all directions. Thus, a Mössbauer spectrometer is simply a device in which the velocity of the source is swept and correlated with the gamma ray intensity at the detector.

Hyperfine Interactions

Hyperfine interactions between the nucleus and its surrounding electronic environment produce slight shifts and splittings in the nuclear energy levels. These shifts and splittings are frequently smaller than the separation of the levels by one part in 10^{11}, but the resolving power of the Mössbauer effect makes possible their observation. The results of such observations can be used to gain information about the electronic environment of the nucleus (30,31,32,33).
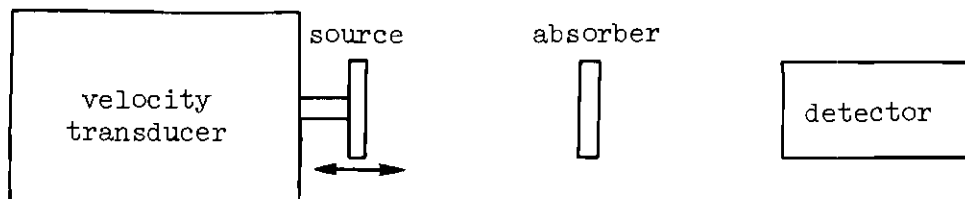
a) Mössbauer Spectrometer.
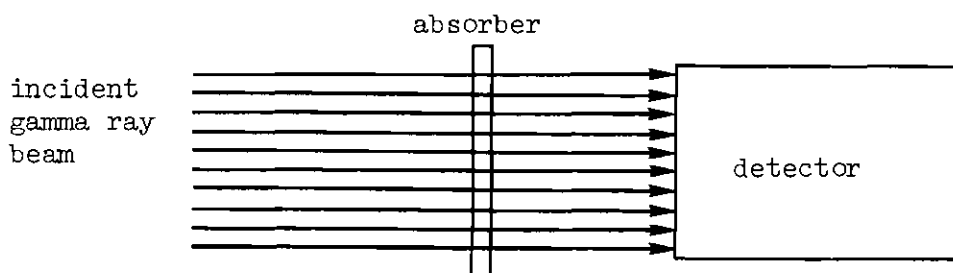
b) Non-resonant Situation.
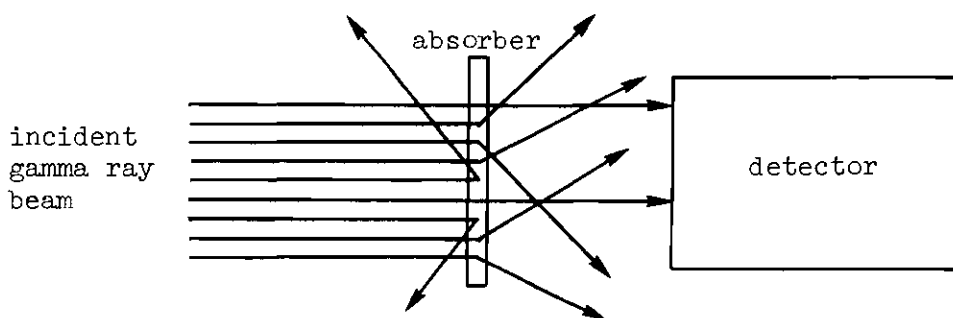
c) Resonant Absorption and Re-emission.

Figure 7. Mössbauer Spectroscopy.

The Effective Magnetic Field. A nucleus with a magnetic moment μ_I and spin $\vec{I}$ will interact with an applied magnetic field H, which can be either an externally applied field or an effective internal field such as exists in ferromagnets. The Hamiltonian describing this hyperfine interaction is

$$\mathcal{K} = - g_I \ \vec{I} \cdot \vec{H} \tag{1}$$

where g_I is the nuclear gyromagnetic ratio μ_I/I. The magnetic field thus splits each nuclear level into $(2I + 1)$ components by removing the spatial degeneracy of the nuclear spin $\vec{I}$. The energy shift of the substate characterized by m_I is

$$\Delta E = - m_I g_I \ H \tag{2}$$

where the direction of H has been taken as the axis of quantization, $\hat{z}$.

For ^{57}Fe, the level diagram for the 14.4 keV transition is shown in Figure 8, along with a typical Mössbauer spectrum for ^{57}Fe in iron metal. The selection rules governing multipole radiation determine which transitions are allowed in this level scheme. Since the 14.4 keV transition is almost purely of the magnetic dipole type (34), six separate transitions corresponding to $\Delta m_I = \pm 1$ or 0 occur. For the case of a Mössbauer absorber which is ideally thin and magnetic, and which has randomly oriented domains, the use of a single
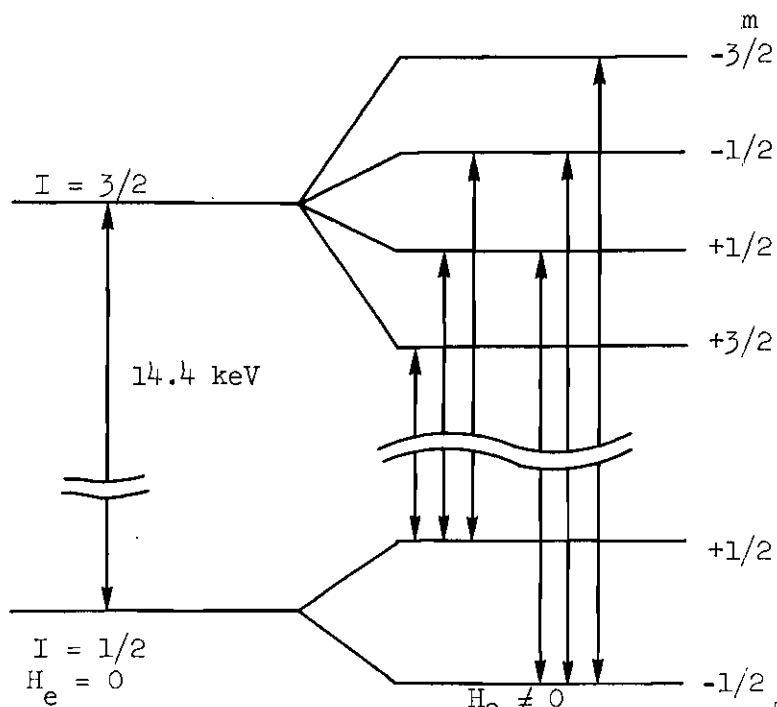
a) Energy Level Diagram of Lowest Two States of ^{57}Fe.
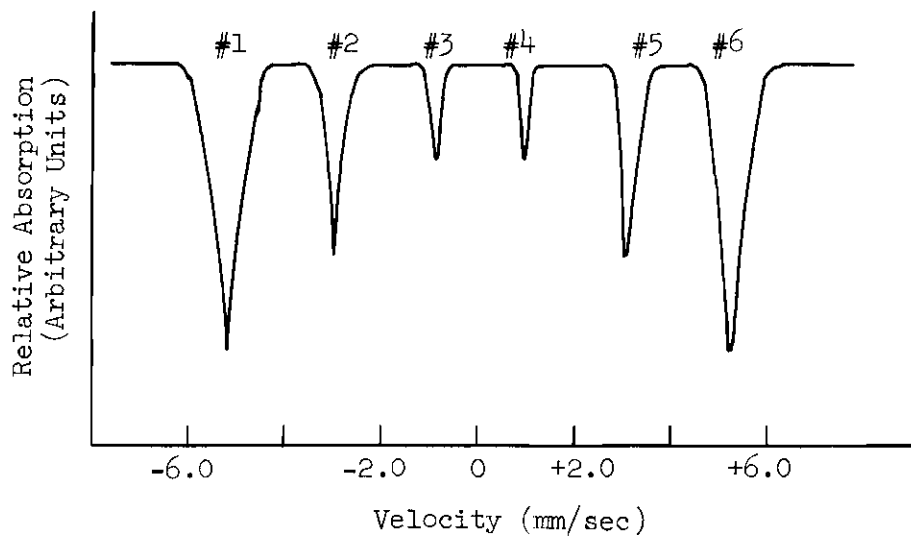
b) Typical Mössbauer Spectrum for ^{57}Fe in Iron Metal.

Figure 8. Level Diagram and Mössbauer Spectrum for ^{57}Fe.

line source will result in a six line spectrum with intensity ratios

for the lines of 3:2:1:1:2:3, as shown in Figure 8b. The effective

magnetic field can be precisely determined from the degree of energy

separation of the lines.

The origin of this large, negative effective magnetic field

may be seen by considering the general Hamiltonian for the interaction

between one atomic electron and the magnetic moment of its nucleus

$$\mathcal{H}_M = -\, g_e g_I \,\, \vec{I} \cdot \left\{ \frac{\vec{l}}{r^3} + \left(\frac{3\vec{r}(\vec{s}\cdot\vec{r})}{r^5} - \frac{\vec{s}}{r^3} \right) + \frac{8\pi\vec{s}\,\delta(\vec{r})}{3} \right\} \tag{3}$$

where g_e is the electron gyromagnetic ratio, and where $\vec{l}$, $\vec{r}$, and $\vec{s}$

are the electron angular momentum, position, and spin vectors,

respectively (35). The effective magnetic field at the nucleus due

to this single electron is

$$\vec{H}_e = g_e \left[\frac{\vec{l}}{r^3} + \left(\frac{3\vec{r}\,(\vec{s}\cdot\vec{r})}{r^5} - \frac{\vec{s}}{r^3} \right) + \frac{8\pi\vec{s}\,\delta(\vec{r})}{3} \right]. \tag{4}$$

The first and second terms are zero for s-electrons and represent the

interaction of the electron orbital momentum with the nucleus and the

dipole-dipole interaction between the nucleus and the electron; in

the case of the transition metals, these terms are small. The third

term is non-zero only for s-electrons and is called the Fermi contact

term. For an s-electron, the effective spin Hamiltonian of the

nucleus can be written

$$\mathcal{H}_M = \left[\frac{16\pi}{3} \mu_B g_I \left\{ |\Psi_{\uparrow s}(0)|^2 - |\Psi_{\downarrow s}(0)|^2 \right\} \right] \vec{s} \cdot \vec{I}, \qquad (5)$$

where $|\Psi_{\uparrow s}(0)|^2$ and $|\Psi_{\downarrow s}(0)|^2$ are the up-spin and down-spin densities, respectively, of the s-electrons at the nucleus (36,37). Thus H_e is sensitive to changes in the unbalanced spin density of the s-electrons in the vicinity of the nucleus.

In ferromagnetic iron, the main contribution to the effective magnetic field comes from a polarization of the 1s, 2s, and 3s electrons (called the "core" electrons) by the aligned 3d electrons (37). This polarization results from the differing exchange inter-actions of the core electrons of up-spins and down-spins with the 3d electrons. Slightly different radial distributions of the core electrons for the two spin states are produced. This difference causes an effective field which is large because the s-electron wave functions are large at the nucleus. Watson and Freeman (38,39,40,41) have calculated the effects of core polarization in iron by using Hartree-Fock methods not restricted to the same radial distribution for the two spin states. They obtained a value for H_e of -330 kOe, the experimentally observed value (15,16,17). Also, the core polarization was found to be sensitive to the size and shape of the 3d electron distribution.

In a metal, the contribution to H_e due to the 4s electrons is not well understood (38,41,42,43). They can have a positive contribution to H_e via polarization by the 3d electrons and by admixing into the 3d band and a negative contribution by covalent mixing with the 3d

electron wave functions.

The Isomer Shift. Another hyperfine interaction which can be observed with Mössbauer spectroscopy is the isomer shift, which is sensitive to changes in the s-electron charge density at the nucleus. This effect was first identified by Kistner and Sunyar in 1960 when they observed that the position with respect to energy of the center of a particular Mössbauer spectrum depended on the chemical form of the absorber (44). Changes in the s-electron wave functions in the vicinity of the nucleus will shift the energy of the nucleus slightly through the electrostatic interaction, because the radii of the excited and ground states of the nucleus are different for many nuclides. The isomer shift, IS, is a product of a part dependent only on the nucleus and a part dependent on the electronic environment of the nucleus:

$$IS = F(Z) \frac{\delta R}{R} \left\{ |\Psi_s(0)|_A^2 - |\Psi_s(0)|_S^2 \right\} , \tag{6}$$

where $F(Z)$ is a function only of the nucleus, of atomic number Z, and where R is the radius of an equivalent uniform charge distribution for the nucleus, δR is the change in this radius between the excited and ground states, $\Psi_s(0)$ is the wave function of the s-electrons at the nucleus, and the subscripts A and S on the wave functions identify the absorber and source, respectively (30). For a particular nuclear transition, the nuclear part is assumed to be insensitive to environmental change. The isomer shift will then reflect changes in the total

s-electron density in the vicinity of the nucleus.

Walker, Wertheim, and Jaccarino (45) have interpreted the isomer shift of ^{57}Fe in various materials. They determined the total s-electron density for different 3d electron configurations and the fraction of 4s electrons contributing to the total s-electron density at the nucleus. A plot of these is shown in Figure 9, along with the isomer shift. The isomer shift was calibrated with sodium nitroprusside ($Na_2Fe(CN)_5NO\cdot2H_2O$), which is used as a convenient standard (46). Note that for iron, a _positive_ isomer shift indicates a _decrease_ in the charge density at the nucleus. This is due to the fact that for iron the excited nucleus has a smaller radius than does the ground state nucleus. The wave functions of the core s-electrons are insensitive to changes in the chemical environment of their particular atom (30). Figure 9 shows that an increase in the isomer shift can be brought about either by a decrease in the total number of 4s electrons or by an increase in the number of 3d electrons, which effectively shield the nucleus from the 4s electrons. The isomer shift of ^{57}Fe in pure iron metal establishes that the electronic configuration in this case is equivalent to $3d^7 4s^1$.

Quadrupole Splitting. If a nucleus possesses a quadrupole moment, it will interact with any electric field gradient present at its position. This is the basis for the observation of quadrupole splitting by Mössbauer spectroscopy. The nuclear quadrupole moment tensor Q_{ij} will interact with the electric field gradient $\partial^2 V/\partial x_i \partial x_j$ with energy
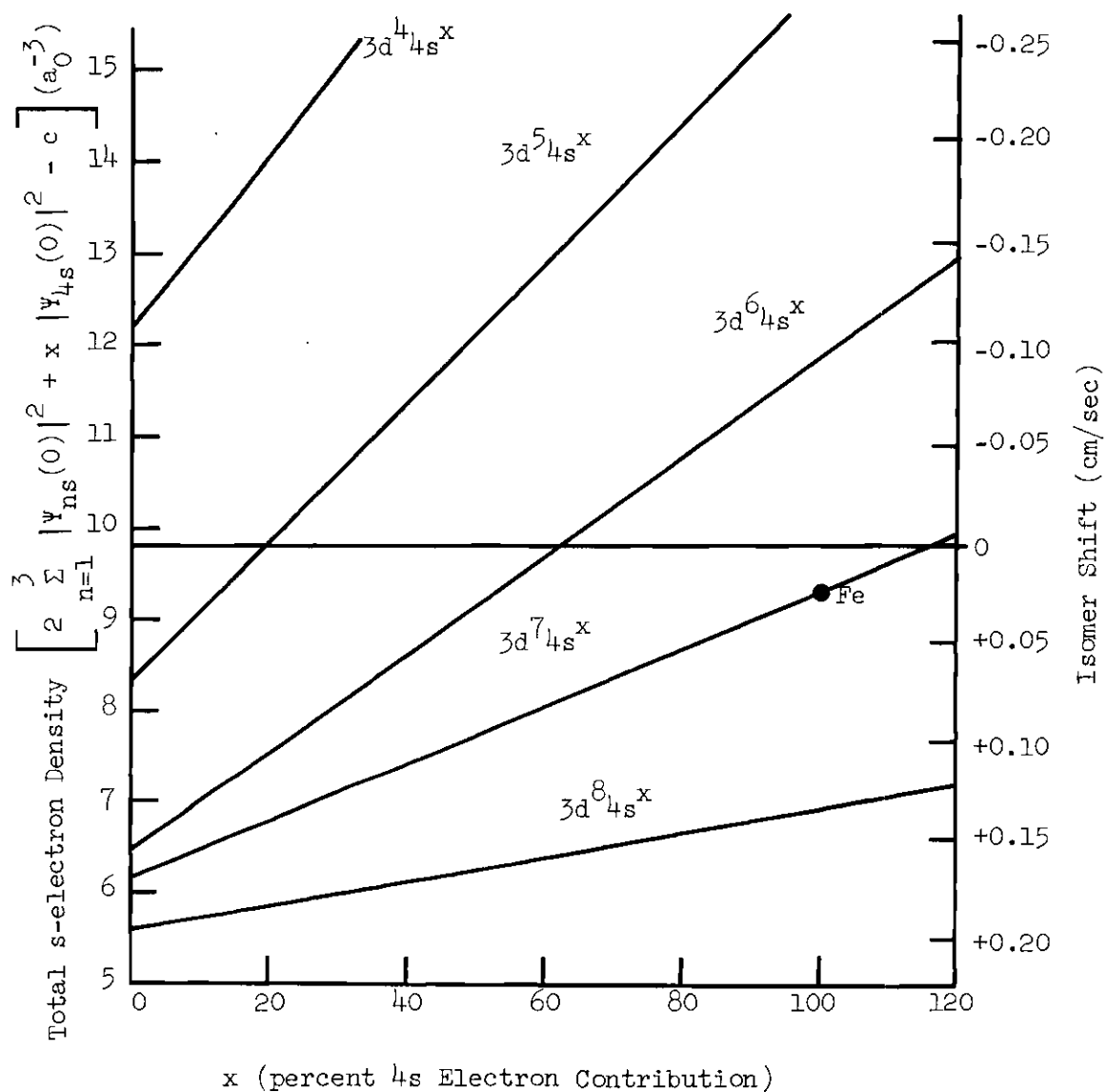
Figure 9. Density of s-Electrons and Isomer Shift, Relative to Sodium
Nitroprusside, versus 4s Electron Contribution for Various
Iron 3d Electron Contributions (45,46). (a_0 = 5.29 x 10^{-11}m
and c = 1.1873 x 10^{-3} a_0^{-3}.)

$$E = - (1/6) \sum_{ij} Q_{ij} \frac{\partial^2 V}{\partial x_i \partial x_j} \Big|_o \;, \tag{7}$$

where i and j are summed from one to three and indicate Cartesian coordinates, and where the electric field gradient is evaluated at the nucleus. The quadrupole moment tensor Q_{ij} is defined as

$$Q_{ij} = \int \rho \, (x_1, x_2, x_3 \,)(3x_i x_j - \delta_{ij} r^2)dv \tag{8}$$

where ρ is the charge density of the distribution which causes the moment. It is easy to show that for an electrostatic situation and for cubic symmetry, the quadrupole interaction will be zero.

The 14.4 keV level of ^{57}Fe has a quadrupole moment and the quadrupole interaction can be observed with this nuclide (30). In iron alloys, the main contribution to the quadrupole splitting of the nucleus of an iron atom is expected to be due to the charge distribution of the neighboring atoms. However, no detailed results of quadrupole splitting studies on alloys have been reported.

Line Shape. For an infinitely thin, pure iron absorber, the Mössbauer absorption lines have a Lorentzian line shape. However, fluctuations in local environment, such as occur in atomically disordered alloys, may appreciably modify the shape and width of these lines. For a particular alloy sample, the Mössbauer spectrum is a superposition of the spectra of all of the Mössbauer nuclei. If the hyperfine interactions of these nuclei with their surroundings are

dependent on local environment, then this will be reflected in the width of the absorption lines (47). Broad lines indicate that the individual iron atoms are experiencing different local environments, while narrow lines indicate that each iron atom has approximately the same local environment.

CHAPTER II

EXPERIMENTAL APPARATUS AND PROCEDURE

Conventional methods of Mössbauer spectroscopy and data

analysis, modified for increased precision of the results, were

coupled in this research with unique sample preparation. This

preparation was critical to the control of atomic configuration and

is given in detail in the following section.

Sample Preparation

Alloys of 25, 40, 50, 60, and 75 percent cobalt in iron were

prepared from the elements by melting in an arc furnace. Iron and

cobalt of 99.999 percent purity were obtained in rod form from the

United Mineral and Chemical Corporation. The weights of iron and

cobalt necessary for each particular composition were determined with

an accuracy of 0.01 percent using a standard chemical laboratory

balance. These amounts were then melted together into an alloy ingot

using a Materials Research Corporation argon arc furnace, model

number AF-92c. The furnace was sealed, evacuated, and flushed with

argon gas. The back-fill pressure in the furnace was approximately

20 in. Hg for the melting process. An electric arc, which was

struck from a nonconsumable tungsten electrode, melted the metals.

After the melting was complete, the furnace was opened and the ingot

was inverted. The entire process was repeated several times to

produce as uniform a distribution of the iron and cobalt throughout

the ingot as possible.

The alloy was further homogenized by heat treating in the following way. Each alloy ingot was first wrapped in tantalum foil, which preferentially absorbs oxygen and minimizes oxidation of the alloy. The ingot and its foil wrapping were sealed in a quartz tube, which was evacuated to 5×10^{-6} torr. The quartz tube and its enclosed ingot were heated at 1200 °C for a week and then cooled to room temperature. The homogenizing temperature used was the maximum to which the quartz tube could be raised without its collapse.

The next step in the process of alloy preparation was the grinding of each ingot into fine powder. Since Mössbauer spectroscopy involves the transmission of low energy (14.4 keV) gamma rays through the sample under study, it is necessary to use either thin foil absorbers or absorbers made of evenly distributed fine powders of an equivalent thickness of material. Because thin foils of the extremely brittle iron-cobalt alloys are difficult to fabricate and effectively heat treat, the fine powder approach was used in this work. Powders of each alloy were made from the ingots using the grinding apparatus shown in Figure 10. An alloy ingot was glued with Duco cement to the level arm, and the lever arm was positioned so that the ingot was in contact with the carborundum (silicon carbide) grinding wheel. Weights were hung from the level arm to increase the pressure of the ingot on the grinding wheel. The timer allowed the motor to run intermittently, thus preventing overheating of the ingot. The resulting powders contained both alloy and carborundum; a simple but tedious magnetic separation procedure enabled the retrieval of
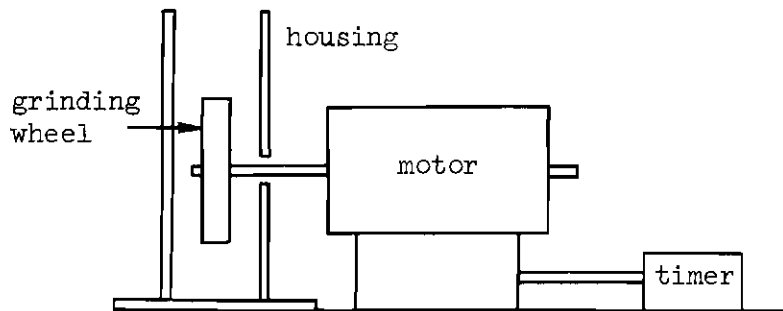
a) Front View of Grinding Apparatus. Alloy ingot and lever arm
   are not shown.
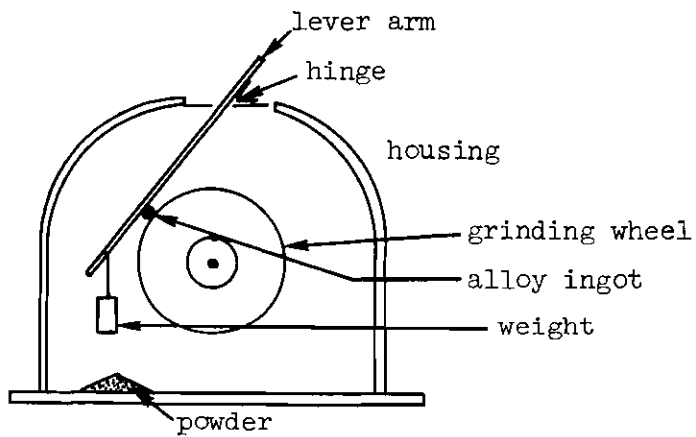
b) Side View of Grinding Apparatus.

Figure 10. Schematic Diagram of the Grinding Apparatus.

the alloy powder from the mixture. The separated alloy powder was passed through a #200 mesh screen, which has 0.0029 ± 0.0002 inch square openings. Besides giving a convenient size of alloy particles, this sifting served to further isolate the larger carborundum particles. Since carborundum is a refractory material and chemically inert even at high temperature, any carborundum remaining in the alloy powder had no effect on the subsequent heat treatments. Furthermore, since it contains iron only as a minute impurity, the carborundum had a negligible effect on the Mössbauer spectra.

Subsequent heat treatments were designed to produce different states of internal atomic order in the various alloys. Two types of heat treatment were used: a fast quench from a particular temperature and an annealing treatment at 500 °C with a slow cool-down. If a quench is fast enough and uniform enough, the atomic arrangements will be retained in the alloy which are characteristic of the alloy's temperature just before the quench. Because the times for configurational rearrangement at room temperature are so long in iron-cobalt (48,49), the quenched samples could be kept indefinitely without appreciable change in their state of atomic order.

The procedure for a typical fast quench is described in detail below. The amount of powdered alloy used in each sample was equivalent in iron weight to a 0.001 inch thick iron foil of the same area. This amount was weighted out using a standard chemical laboratory balance and mixed with approximately four times as much (by volume) finely powdered, chemical reagent grade SiO_2. This mixture was placed over another layer of SiO_2, which was in the bottom of a high purity,

alumina crucible of approximate dimensions $3 \times \frac{1}{2} \times \frac{1}{2}$ inches. A top layer of SiO_2 powder was then added. The purpose of the SiO_2 powder was twofold: First, by dispersing the alloy particles, it prevented sintering. Second, because of its high heat capacity relative to the amount of alloy, it effectively kept the alloy from cooling appreciably during its passage from the oven center to the ice water of the quenching bath. Once in the water, the fine SiO_2 and alloy powders rapidly dispersed to make excellent thermal contact with the water.

When the crucible and powders were ready, they were placed in the oven tube. Figure 11 shows a schematic diagram of the quenching apparatus. The oven was a Lindberg model number 54266. The crucible was attached to a chain made of #28 gauge chromel wire and placed in the center of the oven tube. The oven tube had a center section made of one inch diameter quartz, a gas inlet tube at one end and flanges at both ends. The gas handling system made possible a steady, controllable flow of dried helium or hydrogen gas through the oven tube. When hydrogen was used, it was passed through the catalytic deoxidizer, an Engelhard Industries 10 cfh Deoxo unit, to remove any oxygen present. A liquid nitrogen cold trap was used to remove water vapor and other condensables from the gas. The gas finally flowed through the oven tube, the quenching fixture, a glass tee, and out of the building through a 1/4 inch diameter copper tube. The chromel chain passed out of the system through a clamped rubber tube attached to one arm of the glass tee; this provided a leak tight seal.

In the quenching procedure, helium gas was first used to flush

cold
trap

catalytic
purifier

chromel
chain

crucible

access
flange

flow
meter

oven
tube

oven

gas
storage
tanks

He$_2$

H$_2$

see Detail A

gas exit

Detail A

quenching fixture

clamp

water

glass flange

beaker
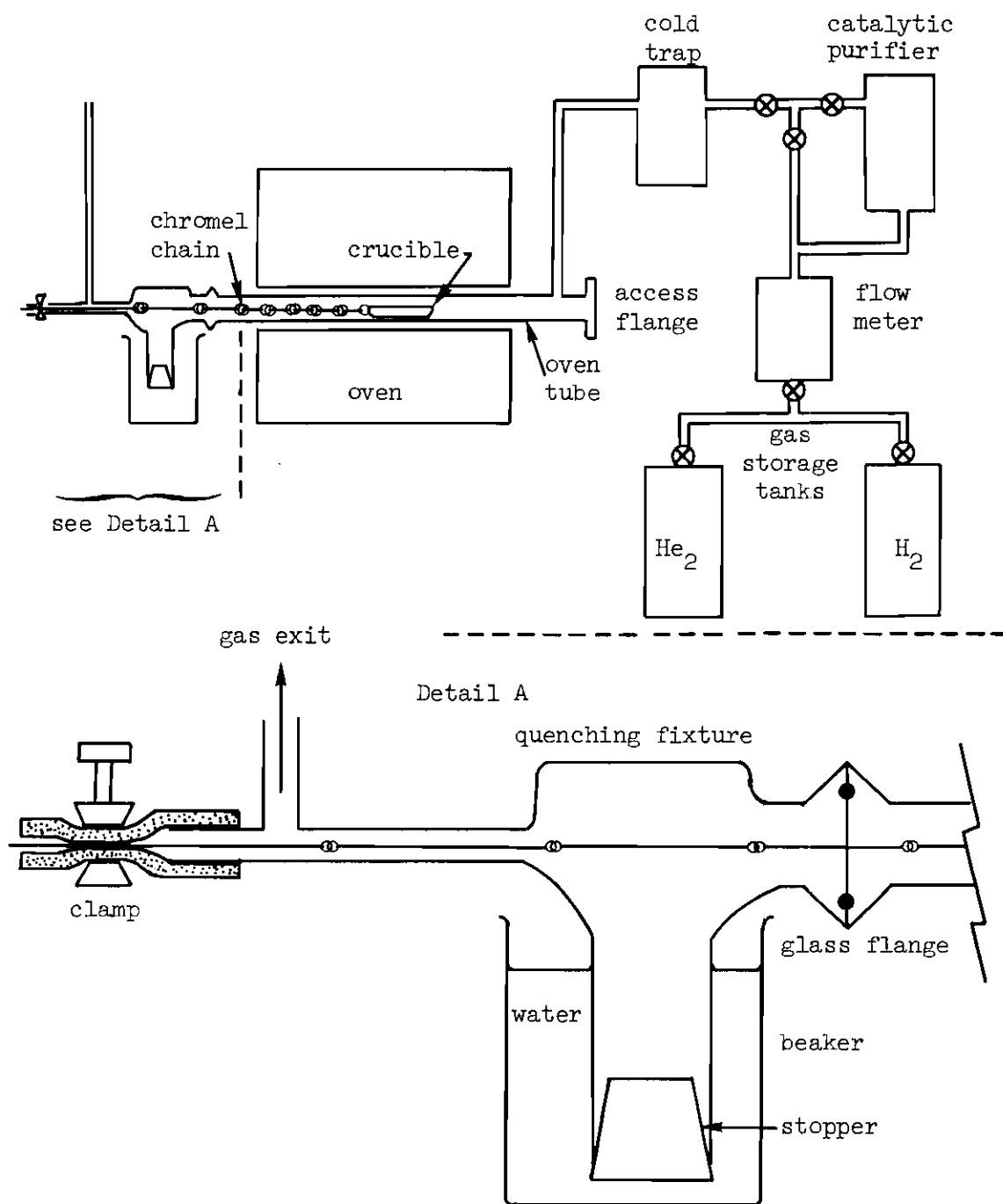
stopper

Figure 11. Schematic Diagram of the Quenching Apparatus.

air out of the system. Next, the cold trap was filled with liquid nitrogen, the helium flow was stopped, and a hydrogen flow of approximately 50 cc/min was started. The oven was turned on with a setting of 500 °C for about one hour; this effectively baked out any oxygen absorbed in the walls of the oven tube and in the crucible. The hydrogen combined with the liberated oxygen and prevented oxidation of the alloy sample. After the bakeout, the temperature in the oven was raised to 850 °C and then lowered in steps to the final temperature from which the quench was made. When thermal equilibrium had been reached (this took more than two weeks for alloy treatments in the 510 °C range), the hydrogen flow was stopped, and a helium flow of one hour was used to flush the system of hydrogen. The rubber tube clamping the chain was next opened; a beaker of ice water was raised around the lower extension of the quenching fixture; and the rubber stopper was removed from the lower opening of the quenching fixture. Then the chromel chain was pulled, dumping the crucible and its contents into the ice water and accomplishing a fast quench. Distilled water, which had been boiled to remove absorbed oxygen and then cooled under nitrogen to prevent re-absorption of oxygen, was used for the quenches.

Fast quenches from above the order-disorder transition temperature were made on a sample of each of the alloy concentrations studied. In addition, a series of eighteen separate quenches were made on Fe(50-50)Co samples over a temperature range of 510 °C to 850 °C, encompassing both the order-disorder transition at 730 °C and the "550 °C anomaly."

Annealing treatments were also made on samples of each alloy composition. The sample of alloy powder was placed in one of the high purity alumina crucibles; no SiO_2 powder was used, since the temperature of anneal was too low for sintering to occur. The crucible was placed in the center of the oven tube. The quenching fixture and the glass tee were replaced with a direct connection between the oven tube and the 1/4 inch diameter copper gas exit tube. With the crucible in the oven tube, basically the same procedure was followed as that for a fast quench, with the exceptions that the temperature was kept at 500 °C for the entire anneal period of 50 hours and then slowly reduced.

Also, a sample of each alloy composition was prepared using powder that had not been heat treated after it was ground. Mechanical deformation such as grinding is known to disorder binary alloys like iron-cobalt (25). Experimental results on these mechanically deformed samples were compared with results on samples fast quenched from above the ordering temperature to determine the effectiveness of the quench method of disordering.

The samples of alloy powders were fabricated into Mössbauer absorbers by mixing each sample with powdered, reagent grade LiOH. This mixture was pressed into a cylindrical pellet about 0.1 inches thick and 5/8 inches in diameter by using a piston-cylinder mold and a hydraulic press. The pellets made in this way had excellent long term stability and mechanical properties.

The Mössbauer Spectrometer

A precision Mössbauer spectrometer was used to obtain spectra of the alloy samples. Figure 12 shows a schematic diagram of this
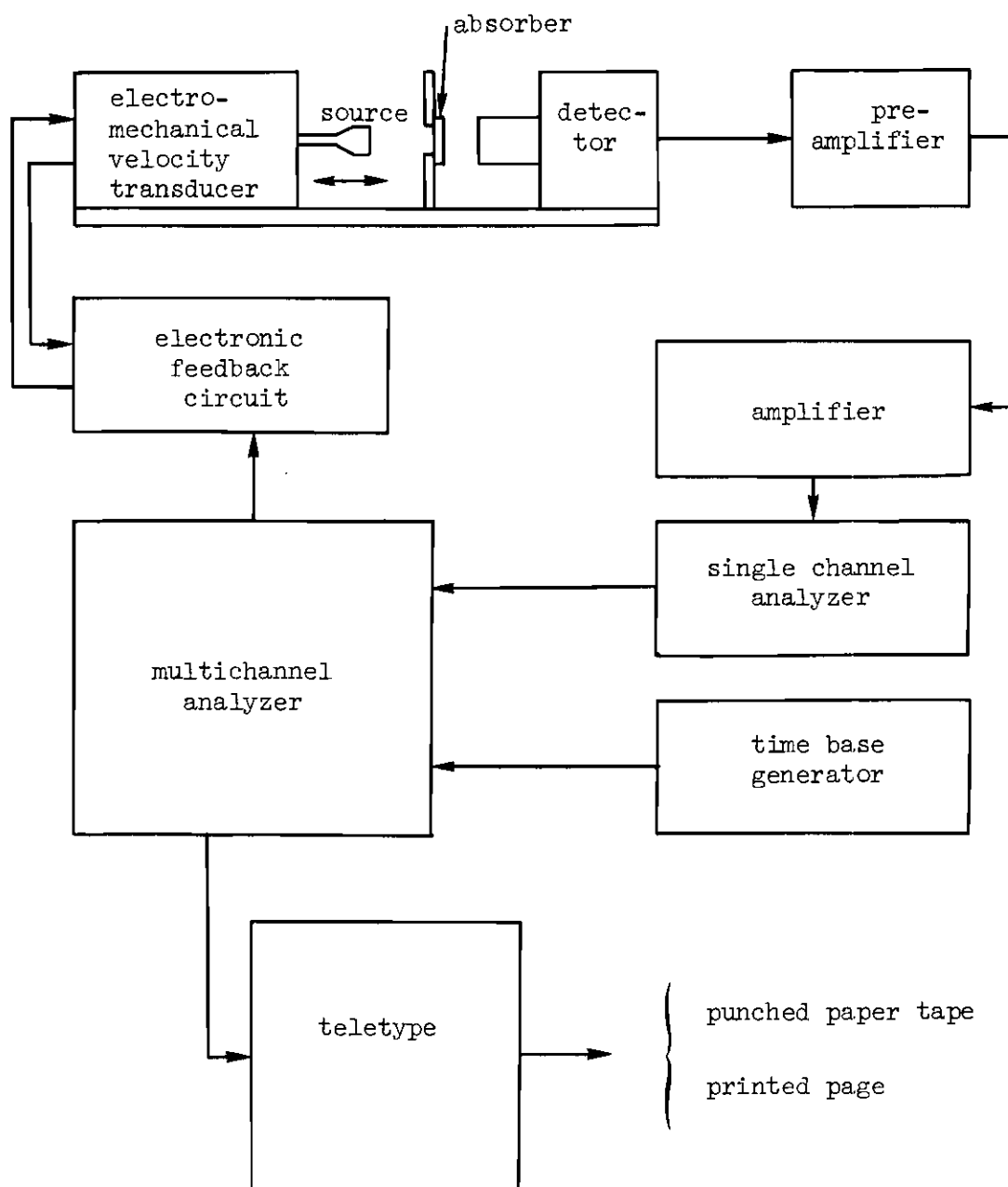
Figure 12. Schematic Diagram of the Mössbauer Spectrometer.

spectrometer. Briefly, the gamma rays from an oscillating source pass

through the absorber and are collected by the detector. Pulses from

the detector are electronically amplified, shaped, and stored in the

400 channels of the multichannel analyzer in a manner directly

related to the velocity of the source. After a sufficient number

of counts are registered in each channel of the multichannel analyzer,

the resulting 400 individual numbers are transferred first to a

punched paper tape and then to IBM data cards. The cards are used

as data input into the computer program utilized for analysis of the

results.

Conventional gamma ray instrumentation was used between the

detector and the multichannel analyzer. The detector itself was

either a NaI(Tl) crystal with a photomultiplier tube, Harshaw Chemical

Company type number K968SHG32K, or a Reuter-Stokes Company $KrCH_4$-filled

proportional counter. The pre-amplifier, amplifier, single channel

analyzer, multichannel analyzer, and time base generator were all

standard catalog items of the Nuclear Chicago Company. The time base

generator allowed the opening of each successive channel of the

multichannel analyzer at time intervals of 0.2 msec; the process was

repreated every 80 msec. The motion of the electromechanical velocity

transducer, or driver, was closely tied to this period by means of

the electronic feedback circuit. The driver, shown in Figure 13,

consisted of two permanent magnets rigidly attached to an aluminum

base plate and of two coils of wire on aluminum forms. Each coil was

situated in the gap of one of the magnets. The coils were connected

by an aluminum rod, which was supported by two phosphor-bronze springs.
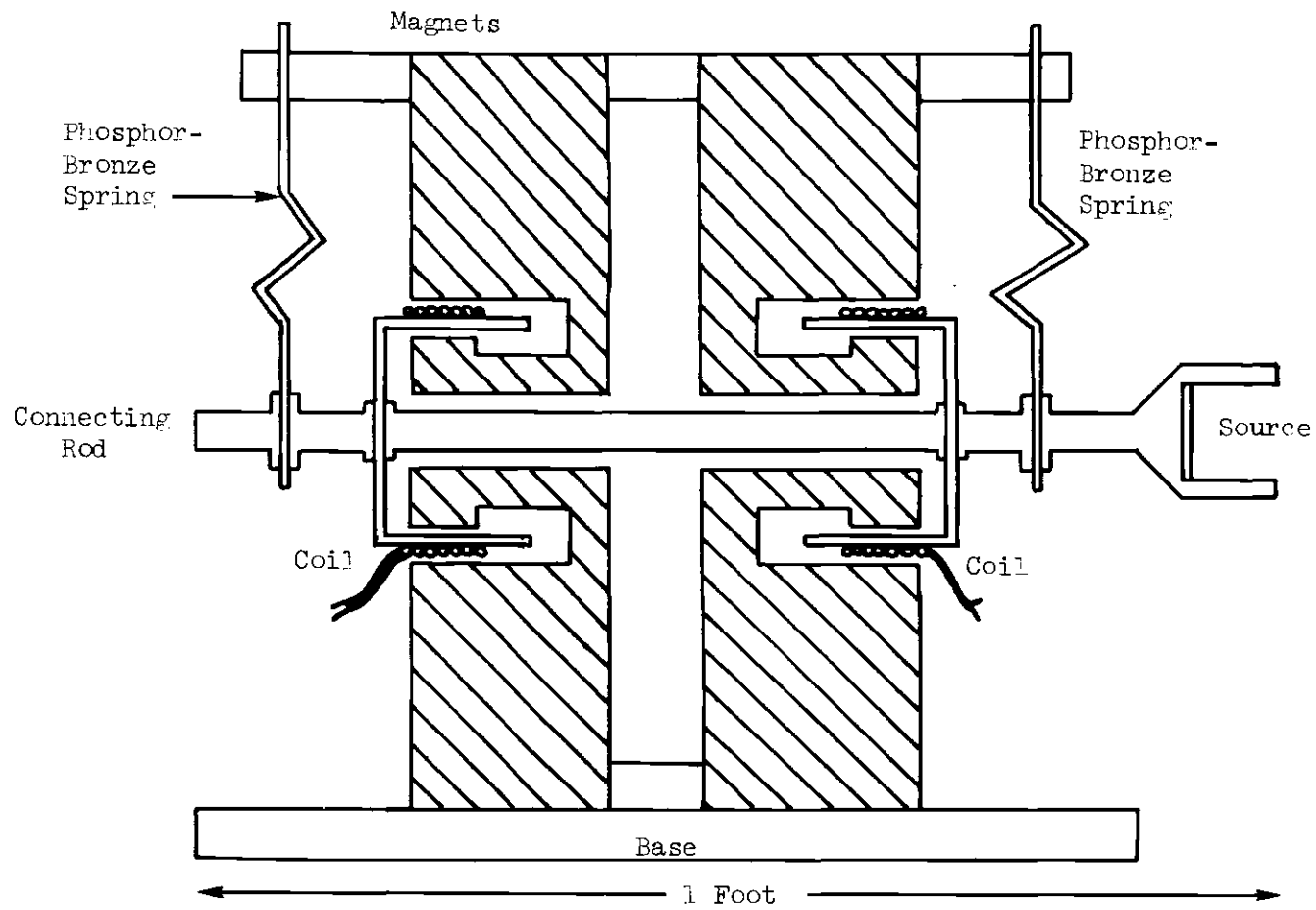
Figure 13. Schematic Diagram of the Electro-Mechanical Velocity Transducer.

These springs allowed motion parallel to, but not perpendicular to, the axis of the rod. On one end of the rod was mounted the radioactive source of the 14.4 keV gamma rays, a 0.001 inch thick copper foil with ^{57}Co diffused into it. One of the two coils was used to move the rod; the force on the coil was proportional to the current passed through it. The other coil served as a velocity detector; as it moved in its magnet gap, a voltage signal which was proportional to the velocity was generated. A crude step function of the same period and phase as that of the storing process was extracted from one of the address bistables of the multichannel analyzer and fed into the electronic feedback circuit. This circuit squared the step function, coverted it into a triangular wave of the same period and phase, compared the triangular wave with the signal of the driver's velocity detector coil, and fed a corrected triangular wave into the driving coil. The result was a very accurate, constant-acceleration motion of the radioactive source, with a period and phase directly related to the manner in which each of the 400 channels of the multichannel analyzer was opened. This in turn allowed a very precise velocity versus absorption spectrum to be obtained. Each spectrum typically involved a counting time of about 24 hours to accumulate sufficient counts (about 500,000 counts per channel) for the desired statistical accuracy. A Teletype, model 33TC ASR, was used to transfer the data to a punched paper tape and printed page.

Data Analysis and Calibration Procedure

The IBM data cards of each spectrum were used as input into a

standard least-squares computer program which fitted the spectrum to six Lorentzian lines. The output of the program consisted of the center and half-width at half maximum of each of the six absorption lines, plus the variance of each of these values.

An iron foil enriched to 90 percent ^{57}Fe was used for calibration purposes. A spectrum of this foil was taken immediately before and after each sample spectrum. The effective field of this foil was taken to be -330 kOe (15,16,17) and the velocity separation between the lowest and highest energy lines was taken to be 10.657 mm/sec (34). From these the necessary calibration conversion factors connecting channel number with velocity and magnetic field were obtained. A typical conversion factor was 0.07879 ± 0.00006 mm/sec//channel. For a sample spectrum to be considered acceptable, the calibration spectra taken adjacent to it were required to agree in their outer-line separation to better than 0.2 percent, although most agreed to within 0.05 percent. The errors were calculated using the variances obtained from the least-squares fitting analysis.

Spectra of the enriched iron foil were also compared with spectra of high purity powdered iron samples which were thermally treated and made into absorbers with the same methods used for the alloy samples. No effects on the hyperfine interactions due to these preparation methods were found in the pure iron spectra.

CHAPTER III

EXPERIMENTAL RESULTS AND DISCUSSION

Room temperature Mössbauer spectra were taken on the iron-cobalt alloy samples which were prepared using the thermal and mechanical treatments described in Chapter II. The high precision Mössbauer spectrometer was used to determine the effect of changes in local atomic environment on the ^{57}Fe effective magnetic field, isomer shift, quadrupole splitting, and line shape. The atomic environments of the iron atoms were effectively changed by two methods: (1) varying the alloy composition between 25 and 75 percent cobalt, and (2) varying the degree of atomic configurational order between complete order and complete disorder. A set of Fe(50-50)Co samples, which were prepared with atomic configurations representative of a series of temperatures between 510 °C and 850 °C, were also studied. Neutron diffraction measurements made at the Georgia Tech Neely Nuclear Research Center were used to determine unambiguously the state of atomic order in selected samples. A complete tabulation of the Mössbauer data is given in the Appendix.

Order-Disorder and Composition Dependence

Effective Magnetic Field Results

The composition and atomic order dependence of H_e is shown in Figure 14. The most striking feature of this data is the decrease of H_e on going from the disordered to the ordered states. This is
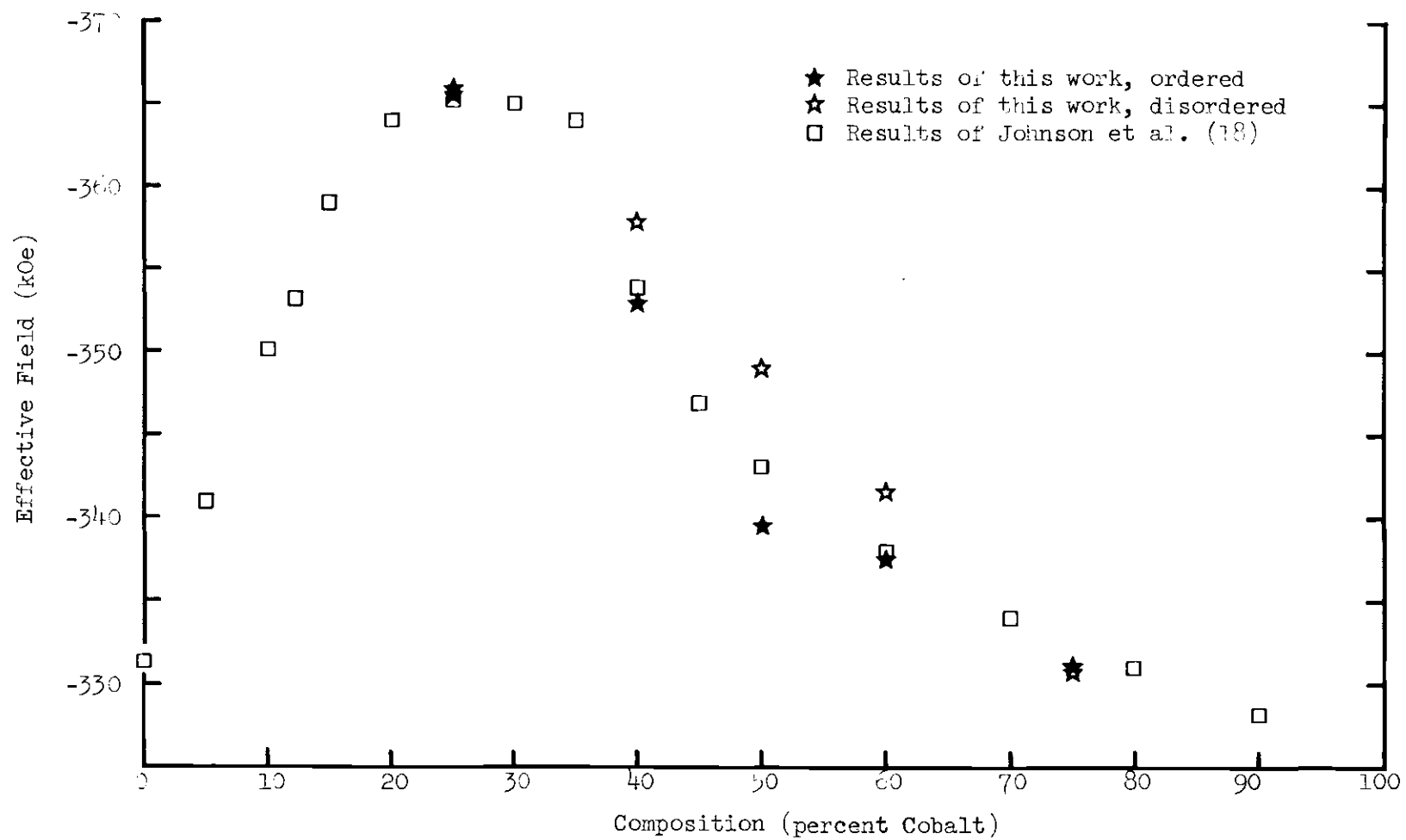
Figure 14. Effective Magnetic Field at the Iron Nuclei as a Function of Composition. (The calculated errors for the results of this work are smaller than the size of the symbols.)

exactly opposite to the effect reported by Johnson et al. (19) and
opposite to the direction of the change of the iron magnetic moment
(Figure 3, page 6). In the concentration region 25-75 percent
cobalt, it is seen that increasing the number of cobalt neighbors to
each iron atom, either by ordering or by increasing the concentration
of cobalt, has the effect of decreasing the magnitude of H_e.
However, in the 0-25 percent cobalt region, the opposite is true.
The overall composition dependence of the effective field in disordered
alloys is similar to that of the average magnetic moment per atom
(Figure 3). The magnitude of H_e is increased by 37 kOe at 25 percent
cobalt over the pure iron value. Above 25 percent cobalt, H_e decreases
in magnitude with added cobalt until it is equal to the pure iron value
at 75 percent cobalt. The maximum effect due to ordering occurs at
50 percent cobalt and represents a difference in magnitude of 10 kOe
between complete order and complete disorder.

The negative sign of the effective field was not directly
determined. The sign of H_e for pure iron is known to be negative (16),
and it can be directly inferred from the data in Figure 14 that the
effective field does not change in sign as a function of composition.

The values of H_e for samples disordered by mechanical deformation
(MD) and by fast quenching from above the ordering temperature (FQ)
agreed within the error limits for each composition studied. Since
neutron diffraction measurements indicated that the MD samples had no
measurable long range order, the conclusion is drawn that the method
used for disordering by deformation is equivalent to the method of
disordering by fast quenching, as indicated by H_e. Neutron diffraction

measurements were also used to determine that the annealed
Fe(50-50)Co sample was highly ordered.

Isomer Shift and Quadrupole Splitting Results

The isomer shift results are shown in Figure 15, along with the
quadrupole splitting results. These data are not nearly as precise
as those for H_e, since their magnitude is much smaller in proportion
to the experimental errors. However, several important features are
evident. The curve is similar to that of the effective field. There
is a maximum isomer shift of approximately +0.04 mm/sec relative to
pure iron in the region of 25 percent cobalt, and as the cobalt
concentration is increased above 25 percent, the isomer shift
decreases. Also, the isomer shift is less for ordered samples than
for disordered samples of the same composition, with a maximum
difference of about 0.02 mm/sec occurring at around 50 percent
cobalt. The measurements of this study are more precise than those
of Johnson et al. (18), who report only a positive isomer shift of
magnitude less than the experimental error of ± 0.05 mm/sec. The
observed shifts are approximately the same for samples disordered by
MD and FQ. Note that the calculated error appears to be larger than
the scatter of the results.

As shown in Figure 15, the quadrupole splitting is negligibly
small for all of the samples except perhaps for the Fe(25-75)Co
annealed sample. This is an indication that the electric field
gradient is small in iron-cobalt alloys and is not affected appreciably
by changes in composition or ordering.
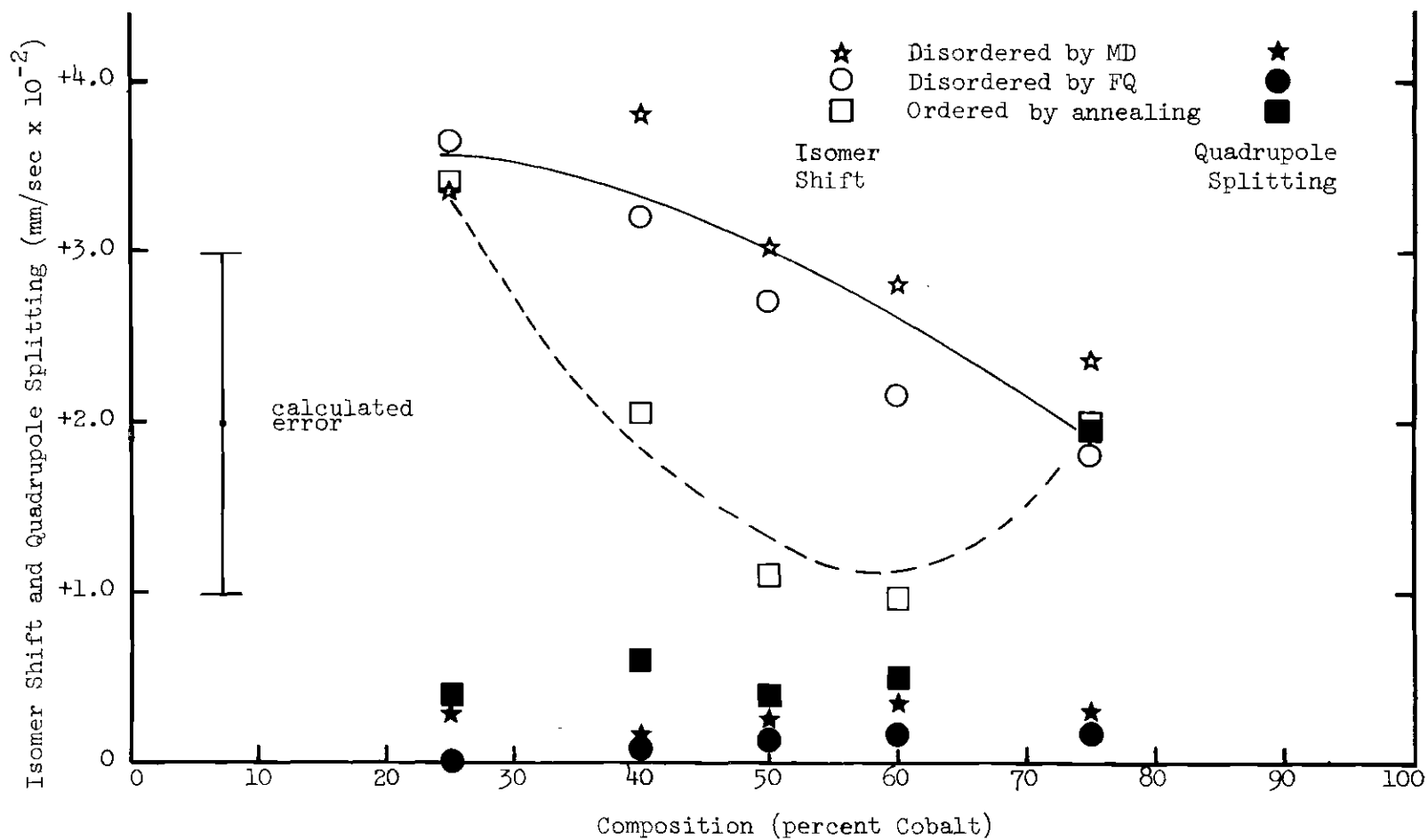
Figure 15. Isomer Shift and Quadrupole Splitting Relative to Pure Iron versus Composition. (MD implies disordering by mechanical deformation; FQ implies disordering by fast quenching from above the ordering temperature.)

Line Shape Results

The half-widths at half maximum (HWHM) for the spectral lines of ordered and disordered samples as a function of composition are shown in Figure 16. Since line broadening effects are larger for the lines of lowest and highest energies than for the other lines, only the HWHM for these lines are given in the figure. The mechanically deformed (MD) samples seem to have slightly broader lines than the fast quenched (FQ) samples for all compositions. Considering the type of strains and dislocations that are thought to occur in the mechanically deformed samples (25), this result is expected.

The line width for the disordered samples is observed to pass through a maximum at 50 percent cobalt while the line width of the ordered samples tends toward a minimum at this composition. A simple statistical argument can be used to predict the distribution of cobalt neighbors about each iron atom. Assuming that cobalt near-neighbors contribute significantly to the hyperfine interactions, it can be shown that a minimum HWHM for ordered alloys, and a maximum HWHM for disordered alloys, occurs at the 50 percent composition, as is observed. Thus the line width behavior shown in Figure 16 indicates a _local_ contribution to the line shape by near neighbor atomic configurations.

The maximum change in line width on going from order to disorder occurs at 50 percent cobalt and is approximately 0.08 mm/sec, which can be compared with the pure iron line width of 0.09 mm/sec (34). The HWHM for lines of the 50 percent cobalt disordered alloy is about 0.30 mm/sec or about 200 percent greater than for pure iron. This is
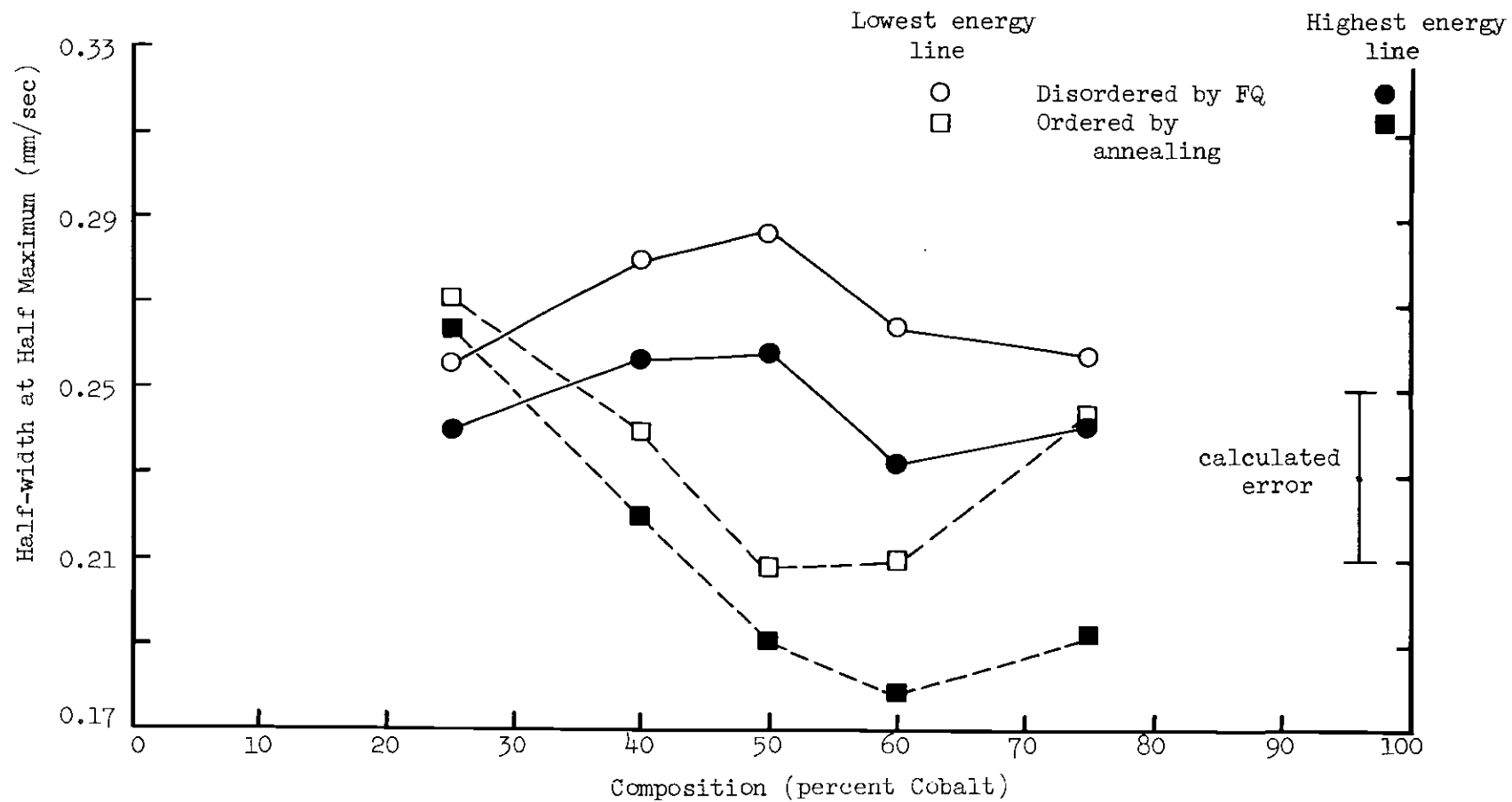
Figure 16. Half-widths at Half Maximum of Mössbauer Spectral Lines as Functions of Composition. (FQ indicates disordering by fast quenching from above the ordering temperature.)

a considerably larger effect than that observed by Johnson et al. (18), who reported a maximum line width broadening for iron-cobalt of only 30 percent greater than for pure iron.

Note that the higher energy lines have a smaller HWHM than do the lower energy lines. Such an asymmetry is observed in the shapes of the other four lines. However, the overall decrease of the line width on ordering is about the same for all of the lines and so the above discussion is not affected by this asymmetry of the HWHM.

Discussion of Order-Disorder and Composition Results

The new findings obtained from the order-disorder and composition studies are: (1) the decrease in magnitude of the effective field on ordering, in contrast to previously reported work (19), (2) the similarity of the composition dependence of the isomer shift and H_e both for ordered and disordered alloys, and (3) the evidence for local contributions to the hyperfine interactions. This information, coupled with the earlier effective field measurements of Johnson et al. (20) in the 0-25 percent cobalt concentration region and with the local magnetic moment data, indicate that there are competing contributions which combine to yield the observed H_e.

Effective Magnetic Field

To characterize these competing contributions to H_e, it is instructive to compare the composition dependence of the effective field with that of the local iron moment, shown in Figure 3, page 6. In the 0-25 percent cobalt region, the increase in the magnitude of H_e with increasing cobalt concentration is accompanied by an increasing

local iron moment, as might be anticipated from other alloy studies
(38); the value for pure iron of -150 kOe/μ_B gives the correct order
of magnitude change of H_e with changing iron moment, in this composition
region.

In the 25-75 percent region, however, the magnitude of the
effective field decreases with increasing cobalt concentration, while
the iron moment continues to increase (Figure 3). H_e decreases still
further with ordering, although the iron moment appears to increase.
Since the number of cobalt first neighbors to each iron atom is
increased either by increasing the cobalt concentration or by increasing
atomic order at a fixed composition, the effect of adding a cobalt first
or second neighbor to an iron atom is to decrease the effective field,
in the 25-75 percent cobalt region. This conclusion is consistent with
the behavior of H_e and the iron moment in the 0-25 percent cobalt
region. The contribution to H_e from the changing iron moment in this
composition region is expected to be much greater than the local effects
for the more dilute cobalt concentrations. Apparently, the local
effects begin to predominate at around 25 percent cobalt.

Further insight into the magnitude of the local contribution to
the effective field may be obtained by analysis of the changes due
to ordering. At the equiatomic composition, for example, the increase
in the iron moment of 0.07 μ_B on going from order to disorder (5)
would imply an <u>increase</u> in the magnitude of H_e of around 10 kOe.[*] The
observed <u>decrease</u> of 10 kOe implies that the local contribution to H_e

---

[*] Similar behavior has been noted in FeNi$_3$ (47).

has a magnitude of 20 kOe between order and disorder at this
composition.

A Phenomenological Treatment. The use of phenomenological
models which are based on the effect of cobalt neighbors on the
effective field would be expected to be of assistance in interpreting
the H_e results in terms of local and competing effects. One such
model is based on the relation for the effective magnetic field at
the nucleus of a particular iron atom:

$$H_e = H_0 + H_{NL} + n_1 H_1 + n_2 H_2 , \qquad (1)$$

where H_0 is the effective field in pure iron (-330.0 kOe), n_1 and
n_2 are the number of cobalt first and second neighbors to the iron
atom, H_1 and H_2 are the contributions of each cobalt first and
second neighbor to H_e, and H_{NL} is the non-local contribution to H_e,
in the sense that it is not dependent on local neighbor effects,
but it does include the effect of changes in the magnetic moment
at the given iron site. Note that additivity has been assumed; this
is commonly done in dealing with dilute alloys (13,14,50,51) and is
sometimes used with concentrated alloys (41). Equation (1) is the
simplest expression possible which takes into account effects due
to first and second near neighbor effects and also due to non-local
effects.

An experimental value for H_e is available for ordered and
disordered samples at each composition studied. Since n_1 and n_2 are
known for a particular composition at complete order and complete

disorder, simultaneous equations can be set up to determine the unknown parameters H_1, H_2 and H_{NL}:

$$H_e^0 = H_0 + H_{NL}^0 + n_1^0 H_1^0 + n_2^0 H_2^0 \quad \text{(order)} \qquad (2)$$

$$H_e^d = H_0 + H_{NL}^d + n_1^d H_1^d + n_2^d H_2^d \quad \text{(disorder)}. \qquad (3)$$

The unknown parameters may be obtained from the experimental data and equations (2) and (3) with certain assumptions. If the parameters are assumed to be independent of atomic order, then the problem is reduced to solving for the three unknowns from two equations. A third relationship involving the parameters is obtained if a statistical ordering model is used with the equations (2) and (3) to calculate the line width of the absorption lines (a detailed discussion of this model given on page 55). The parameters H_{NL}, H_1, and H_2 may then be varied until the experimental line width agrees with the statistical model calculation. From equations (2) and (3), two of the parameters H_{NL}, H_1, and H_2 are known as functions of the third. Figure 17 shows the calculated line width for the disordered Fe(50-50)Co case as a function of H_1, along with the experimentally observed HWHM. It can be seen from the figure that a unique solution is not obtained. The two solutions which reproduce the HWHM data for the equiatomic alloy are (H_1 = +4.3 kOe, H_2 = +2.7 kOe, H_{NL} = -44.1 kOe) and (H_1 = -1.7 kOe, H_2 = -5.3 kOe, H_{NL} = +3.9 kOe). It is apparent that additional assumptions are necessary to eliminate one of these solutions.
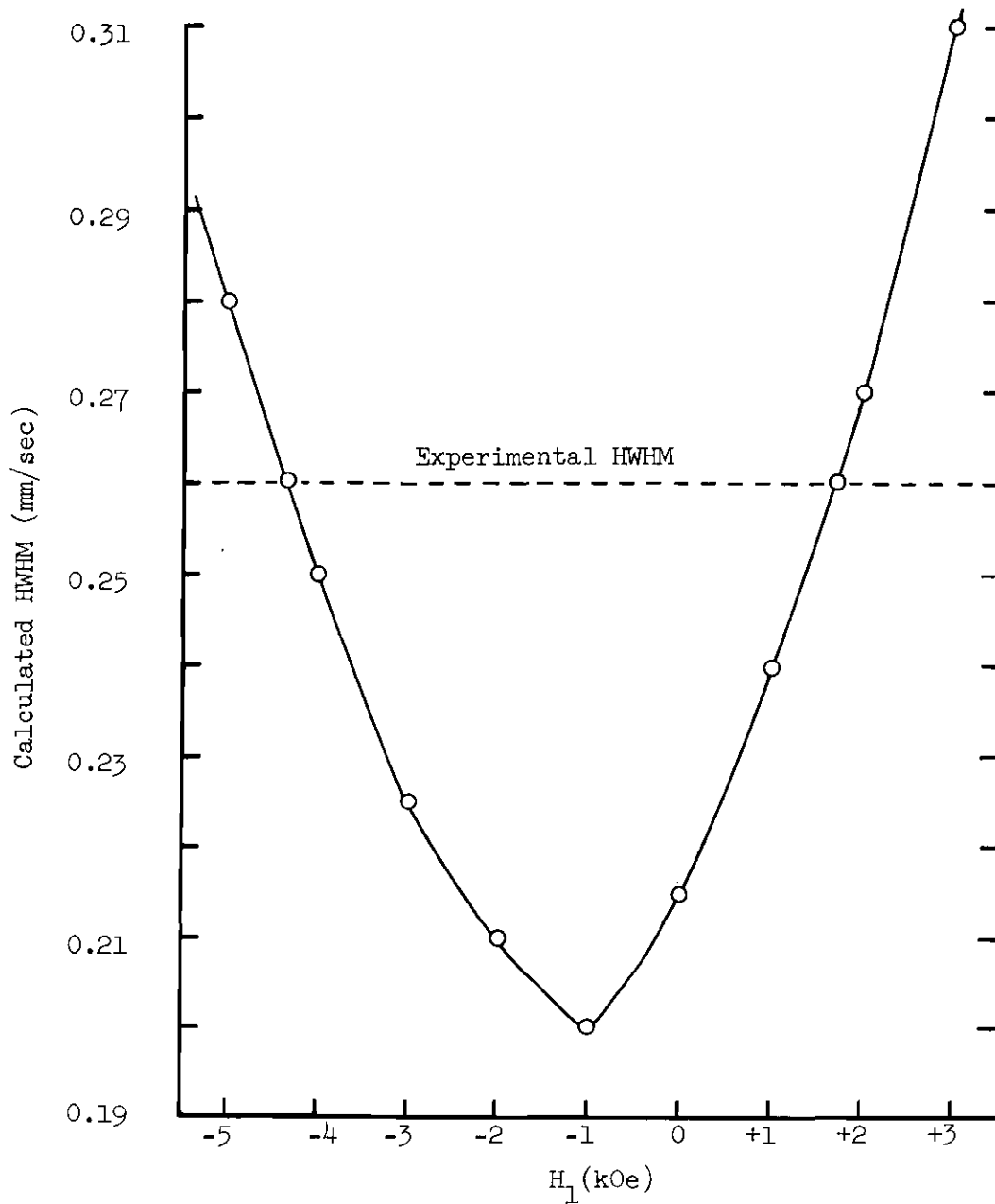
Figure 17. Calculated Half-Width at Half Maximum for Disordered
Fe(50-50)Co versus Values of H_1. (Also shown is the
experimentally observed value. The intersection points
imply (H_1 = +4.3 kOe, H_2 = +2.7 kOe, H_{NL} = -44.1 kOe)
and (H_1 = -1.7 kOe, H_2 = -5.3 kOe, H_{NL} = +3.9 kOe), all
to an accuracy of ±0.5 kOe.)

If it is further assumed that H_1 and H_2 are not dependent on composition, only the first solution can reproduce the measured H_e as a function of composition for both ordered and disordered samples. The positive sign of H_1 and H_2 of this solution infer a reduction in the magnitude of H_e for the addition of a first or second cobalt neighbor to the iron atom; the larger, negative value of H_{NL} may be associated with the dependence of H_e both on changes in the local iron moment and on a long range effect. The positive and negative competing effects predicted from this model are in agreement with conclusions discussed earlier (page 46).

Any simplifications of equation (1) to include only two parameters lead to results which are conflicting and which cannot be used to reproduce the experimental line widths.

Another model frequently used to describe effective field measurements employs the relation

$$H_e = a\mu_{Fe}(c) + b \, \mu_{nn}(c) \, , \tag{4}$$

where a and b are constants, and where the iron magnetic moment μ_{Fe} and the sum of the neighbor moments μ_{nn} are functions of the composition, c. The sum of the neighboring moments in bcc iron-cobalt is given by

$$\mu_{nn} = n_1\mu_{Co}(c) + (8 - n_1)\mu_{Fe}(c) \, , \tag{5}$$

with μ_{Co} being the cobalt moment. The magnetic moments are known from

experimental results (see Figure 3, page 6) and simultaneous

equations for H_c can be set up in the manner described above.

Although this particular model has the advantage of including

additional experimental data, no definite conclusions could be

drawn about the constants a and b.

Conduction Electron Polarization. The observed hyperfine

interactions result from several competing mechanisms which cannot

be quantitatively separated; however, some speculation may be made

of the relation of the hyperfine interactions to conduction

electron polarization (CEP). Phenomena such as superlattice formation,

changes in the lattice parameter, and variations in the 3d-4s mixing

ratio are also expected to contribute, but it is difficult to

determine the extent of these contributions. The relation to the

local magnetic iron moment has already been discussed.

The conduction bands in iron, cobalt, and nickel, and their

alloys with each other, are of mixed 3d-4s electron nature (42,43).

The spin polarization of these bands is expected to be positive,

although the possibility for the existence of a negative CEP in some

parts of the atomic cell in iron is not excluded (52). In fact,

neutron diffraction (53,54,55), positron annihilation (56), and

pressure (57) experiments have indicated a negative CEP in iron.

The results of this work infer a CEP for the 25-75 percent

cobalt range of iron-cobalt which is positive in the vicinity of the

iron nuclei. It has been noted that an increase in the isomer shift

implies a decrease in the volume density of 4s electrons at the

nucleus. Therefore, an increase in the isomer shift will be associated

with an increase in the magnitude of the effective magnetic field

only if the 4s electrons have a net positive spin polarization.

Thus, the close resemblance between the effective field and

isomer shift results is a strong argument for the existence of a

positive CEP. In the 25-75 percent cobalt region, the CEP effect

must be large enough to overcome the effect of the local iron moment,

which increases as H_e decreases. In the 0-25 percent cobalt region,

however, a negative CEP cannot be ruled out since the increase in

iron moment is expected to be the dominant cause of the change in

the effective field.

Atomic Configuration Effects in Fe(50-50)Co

The effects of atomic configurational changes on the hyperfine

interactions in Fe(50-50)Co were determined by using samples quenched

from a series of temperatures between 510 °C and 850 °C.

Effective Magnetic Field Results

Figure 18 shows the results of H_e versus the temperature of

each sample studied just before the quench. Included are the results

for a sample disordered by mechanical deformation (MD) and for a

sample ordered by annealing. The figure displays several interesting

features. Above the order-disorder transition temperature at 730 °C

(1), H_e is seen to have a constant value; H_e for the MD sample agrees

with this value within the error limits. Below 730 °C, H_e decreases

almost linearly down to approximately 550 °C. Below this temperature,

the field has a constant value of -339 kOe, which is equal to H_e for
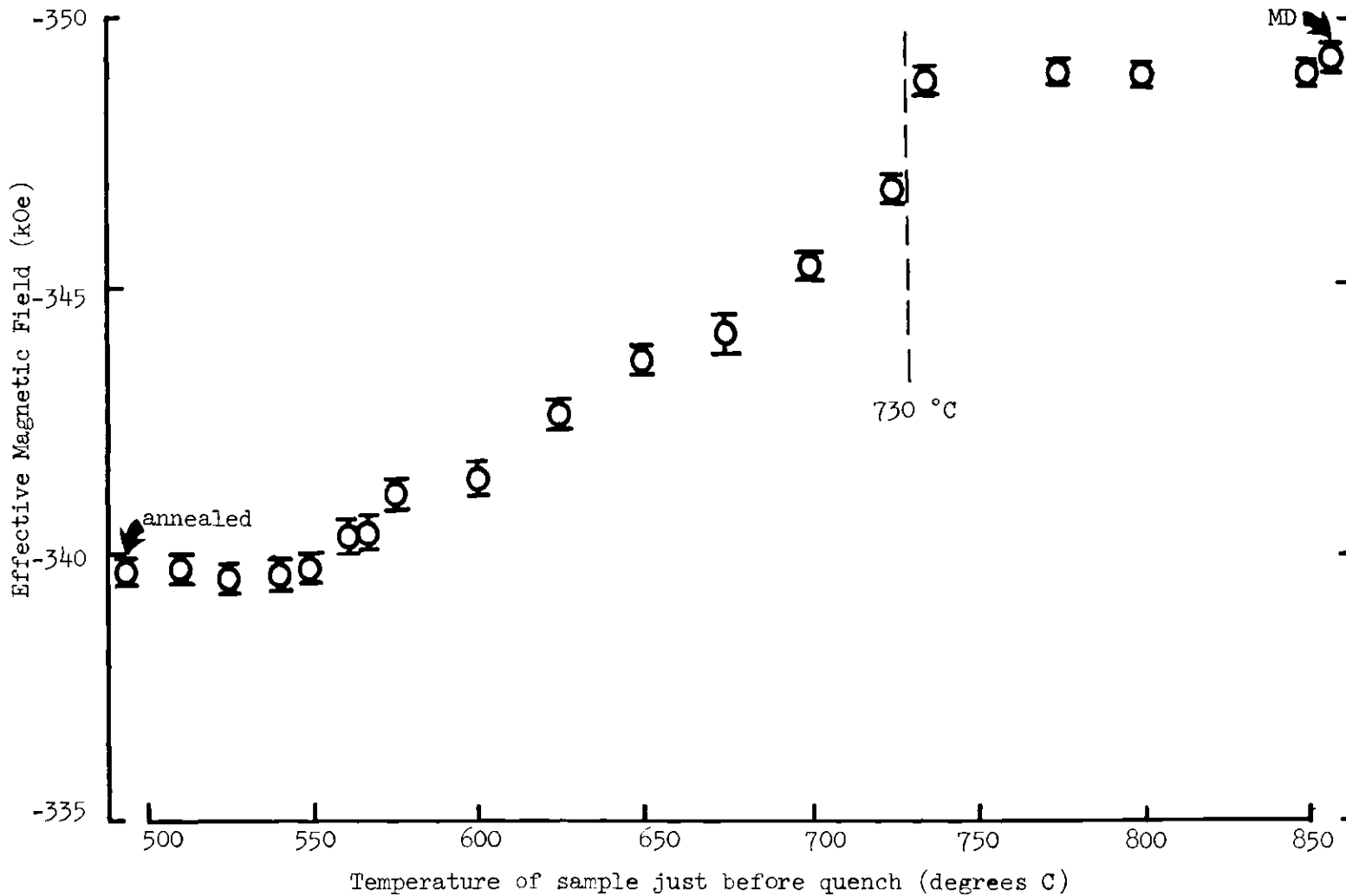
Figure 18. Effective Magnetic Field at the Iron Nuclei versus the Temperature of Each Sample Just Before Quench--Fe(50-50)Co. (Also shown are values for a sample disordered by mechanical deformation (MD) and a sample ordered by annealing.)

the annealed sample.[*] The break in slope near 550 °C is apparently

a manifestation of the "550 °C anomaly."

Figure 19 shows the lowest energy line of an ordered sample

and a disordered sample of Fe(50-50)Co superimposed. The centers of

the two lines are slightly shifted, reflecting the different H_e of

each sample. Also, the ordered sample has a narrower line than does

the disordered sample.

Discussion of the Effective Field Results Using a Statistical Ordering Model

The measured changes of H_e were assumed to be associated with

the local atomic environments, and a statistical representation of

ordering was used to relate the degree of short range order (SRO)

to the quench temperature. The SRO parameters $\{\alpha_i\}$ of Cowley (27,58)

may be used for a quantitative description of the atomic configuration

in a binary alloy. Consider a bcc binary alloy $A_m B_{1-m}$ of atom types

A and B in concentrations m and (1-m), respectively. The probabilities

$\{p_i\}$ that any one of the c_i sites of the ith nearest neighbor shell of

an A-atom is a B-atom are known, and the $\{\alpha_i\}$ are defined with respect

to these probabilities (47). Upon inversion, the probabilities can

be determined from the values of the $\{\alpha_i\}$:

$$p_i = (1-m)(1-\alpha_i) \qquad (6)$$

---

[*] Note that the sample quenched from 510 °C was heated for over two
weeks at temperatures gradually approaching 510 °C, then held at the
quench temperature for several days before the quench. The annealed
sample, on the other hand, was merely heated at 500 °C for two days
and then allowed to cool slowly to room temperature.
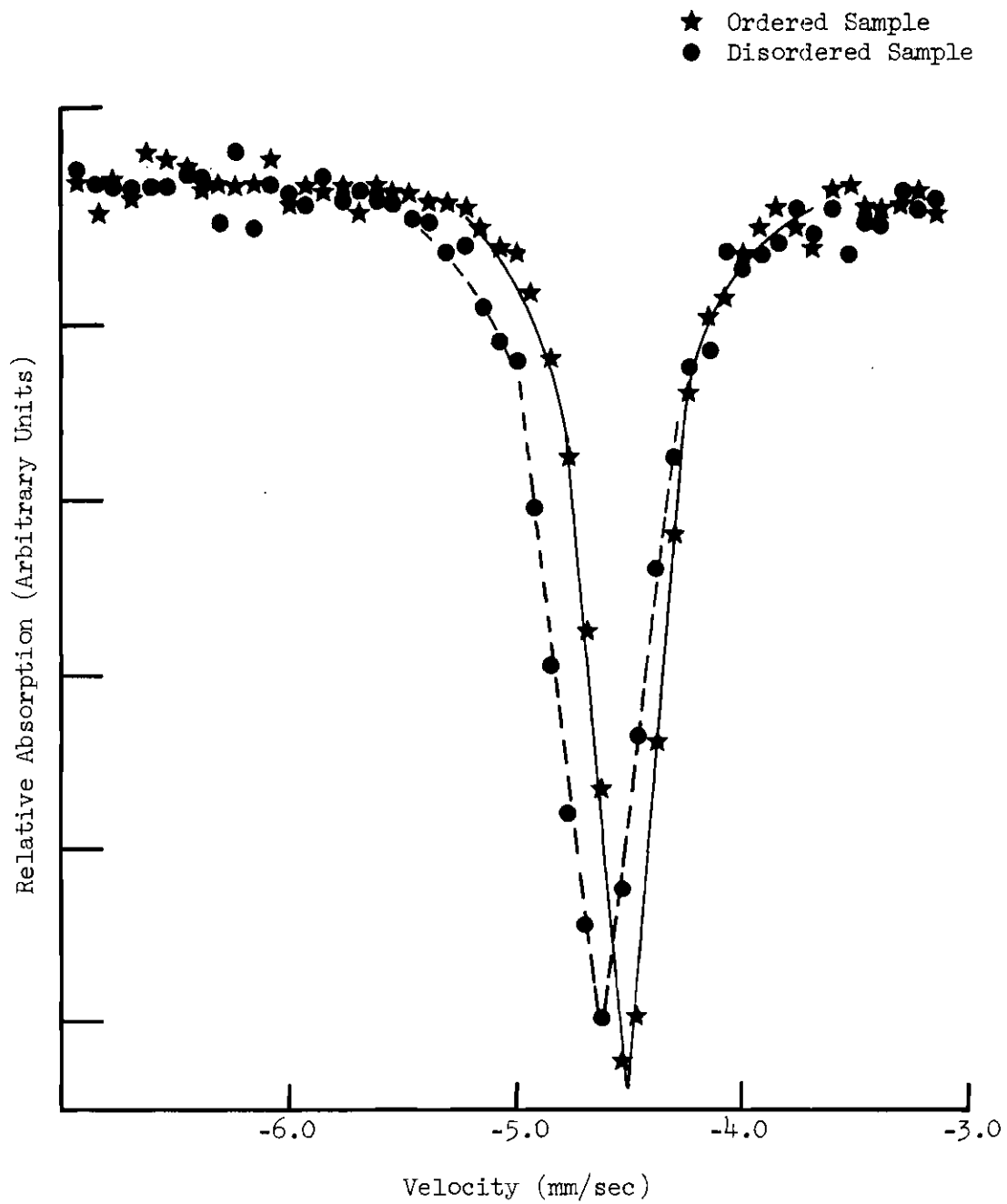
Figure 19.   Relative Absorption versus Velocity for the Lowest Energy
Line of Fe(50-50)Co Ordered and Disordered Samples.

In a disordered alloy, all the $\{\alpha_i\}$ are zero; in an ordered alloy
the $\{\alpha_i\}$ attain their maximum values, which depend on the composition
m and shell i. The normalized SRO parameter $\alpha = \alpha_i/\alpha_{i,max}$ is
usually employed for convenience. The probability of finding
exactly n_i B-atoms among the c_i atoms in the ith shell around an
A-atom is given by the binomial distribution:

$$w_i(n_i) = \binom{c_i}{n_i} (p_i)^{n_i} (1-p_i)^{c_i - n_i}. \tag{7}$$

In the case considered here, bcc Fe(50-50)Co, only the first two
normalized α_i's were used. Their temperature dependence was assumed
to be the same (27) and they were both characterized by the symbol
"α." For the equiatomic alloy, equation (6) is

$$\left. \begin{array}{l} p_1 = (1 + \alpha) \\[2em] p_2 = (1 - \alpha) \end{array} \right\} . \tag{8}$$

Assuming a neighbor-dependent effective magnetic field
$H_e(n_1,n_2)$ for a particular iron atom, such as expressed in equation (1),
the SRO parameter can be used to calculate a Mössbauer spectrum. For
each atomic configuration, the Mössbauer absorption lines are all
Lorentzian in shape and depend on the effective field of the atom
according to

$$L_k(H_e) = \frac{1}{\pi G} \left\{ \frac{1}{1 + \left[\dfrac{H_0 - H_e(n_1,n_2)}{G} \right] 2} \right\} \qquad (9)$$

where k=1, 6 is an index for each line (Figure 8, page 18), and G
is the HWHM of the line for a perfectly ordered sample. The
observed absorption spectrum is a superposition of such lines.
The calculation of a spectrum for a particular value of the SRO
parameter involved summing over the possible near-neighbor
configurations characterized by n_1 and n_2. One obtains for the
composite spectrum:

$$L(H_e) = \frac{1}{\pi G} \sum_{k=1}^{6} c_k \sum_{n_1=0}^{8} \sum_{n_2=0}^{6} \left\{ \frac{w_1(n_1)w_2(n_2)}{1 + \left[\dfrac{H_0 - H_e(n_1,n_2)}{G} \right] 2} \right\}, \qquad (10)$$

where c_k is a constant. H_e can be determined from the position of
the center of one of these lines. The dependence of H_e on the SRO
parameter enters the calculation through the probabilities of
equation (8) and the binomial coefficients.

Figure 20 shows the calculated effective field versus the
SRO parameter. The values of the solution of the phenomenological
analysis (page 49) (H_1 = +4.3 kOe, H_2 = +2.7, H_{NL} = -44.1 kOe) were
used; however, the calculated values were found to be very insensitive
to the particular model used for $H_e(n_1,n_2)$.

From the plot of H_e versus SRO parameter and the plot of H_e
versus quench temperature (Figure 18), the dependence of the SRO
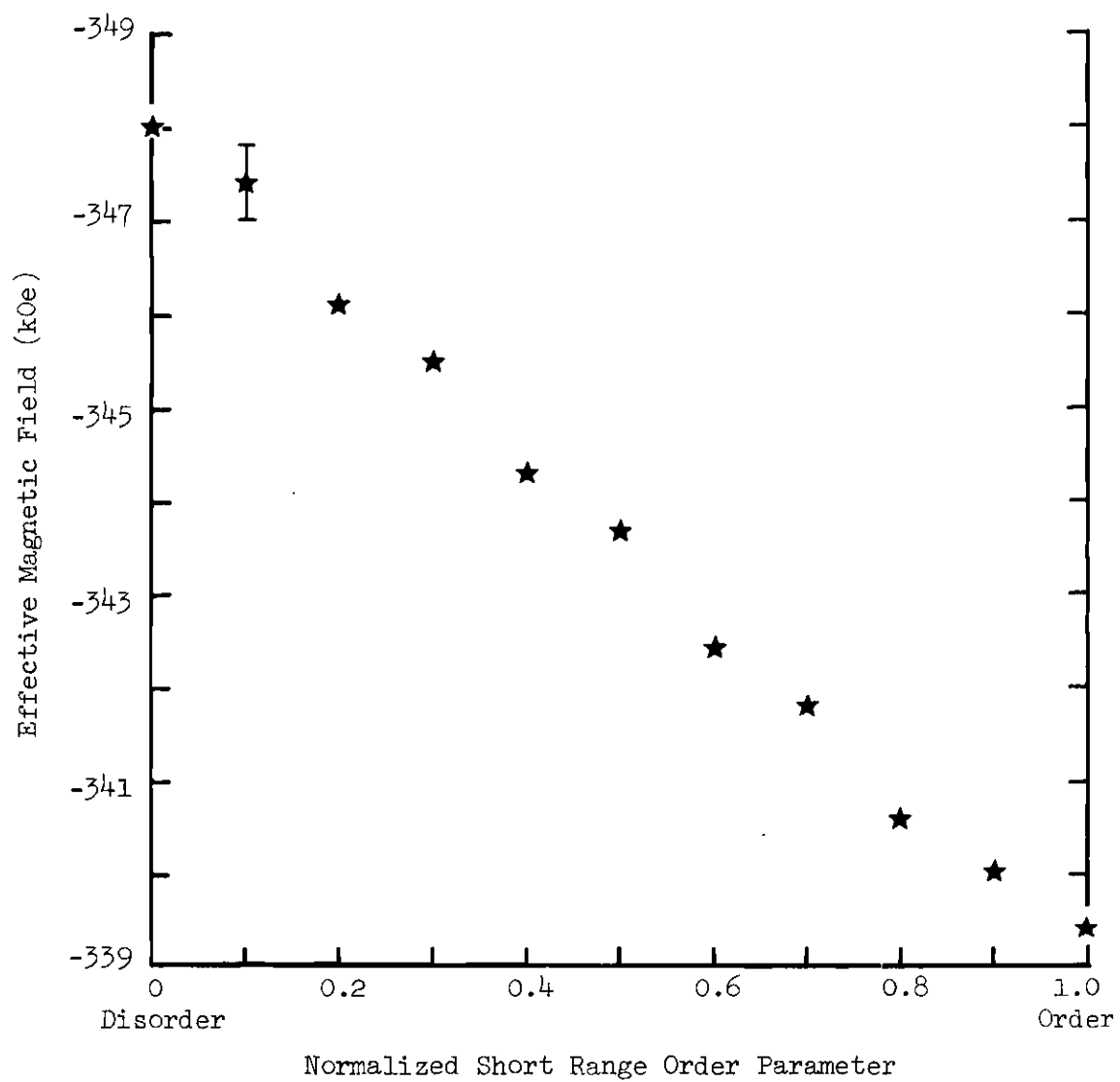
Figure 20. Calculated Effective Field versus Short Range Order Parameter.

parameter on temperature may be deduced. This is shown in Figure 21, along with neutron diffraction results of Lyashenko (59) on the long range order parameter versus temperature. The physical significance of a SRO parameter calculated by the above method must be treated with caution, especially since not all of the contributions to H_e may be associated directly with atomic configurational changes. It is of interest, however, to compare the calculations with the experimental results. Figure 21 shows that above 600 °C the two order parameters appear to have roughly the same temperature dependence. The nature of the curvature at the critical temperature (730 °C) cannot be determined from these data. In the vicinity of 550 °C, the long range order parameter drops suddenly while the calculated SRO parameter increases from a value of about 0.8 to almost complete order in a narrow temperature range. The relationship of the changes in the order parameters to each other is not understood and, in fact, the drop in the long range order does not yet have an explanation.

Isomer Shift and Quadrupole Splitting Results

Figure 22 shows the configurational temperature dependence of the isomer shift and quadrupole splitting for Fe(50-50)Co. Also shown are the results for a sample which was disordered by mechanical deformation (MD) and for a sample ordered by annealing. The isomer shift has a dependence similar to that of H_e, although the data are much less precise. The quadrupole splitting is not measurably affected by configurational changes.

Line Shape Results

Figure 23 gives the results for the dependence of the HWHM on
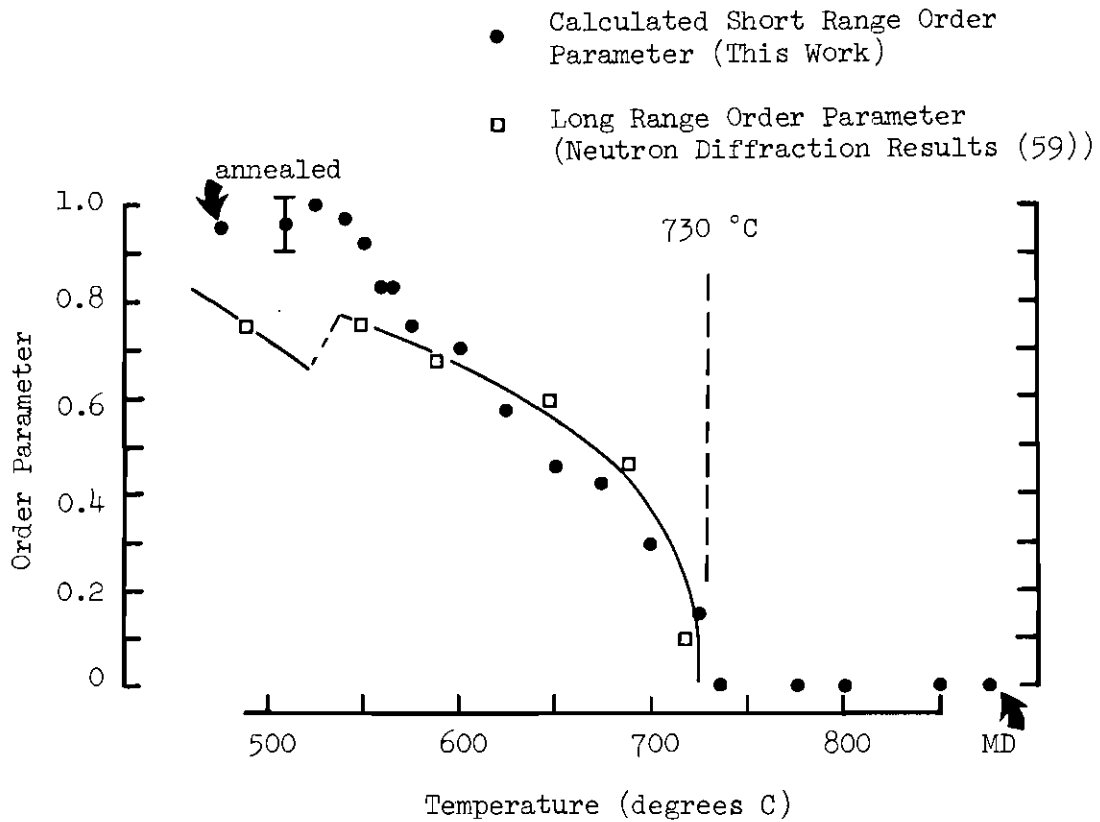
Figure 21. Order Parameter for Fe(50-50)Co versus Temperature.
(Results are shown for the calculated short range order
parameter versus quench temperature (this work) and for
the long range order parameter versus sample temperature
(neutron diffraction results (59). Also shown are
results for an annealed sample and a sample disordered by
mechanical deformation (MD).)
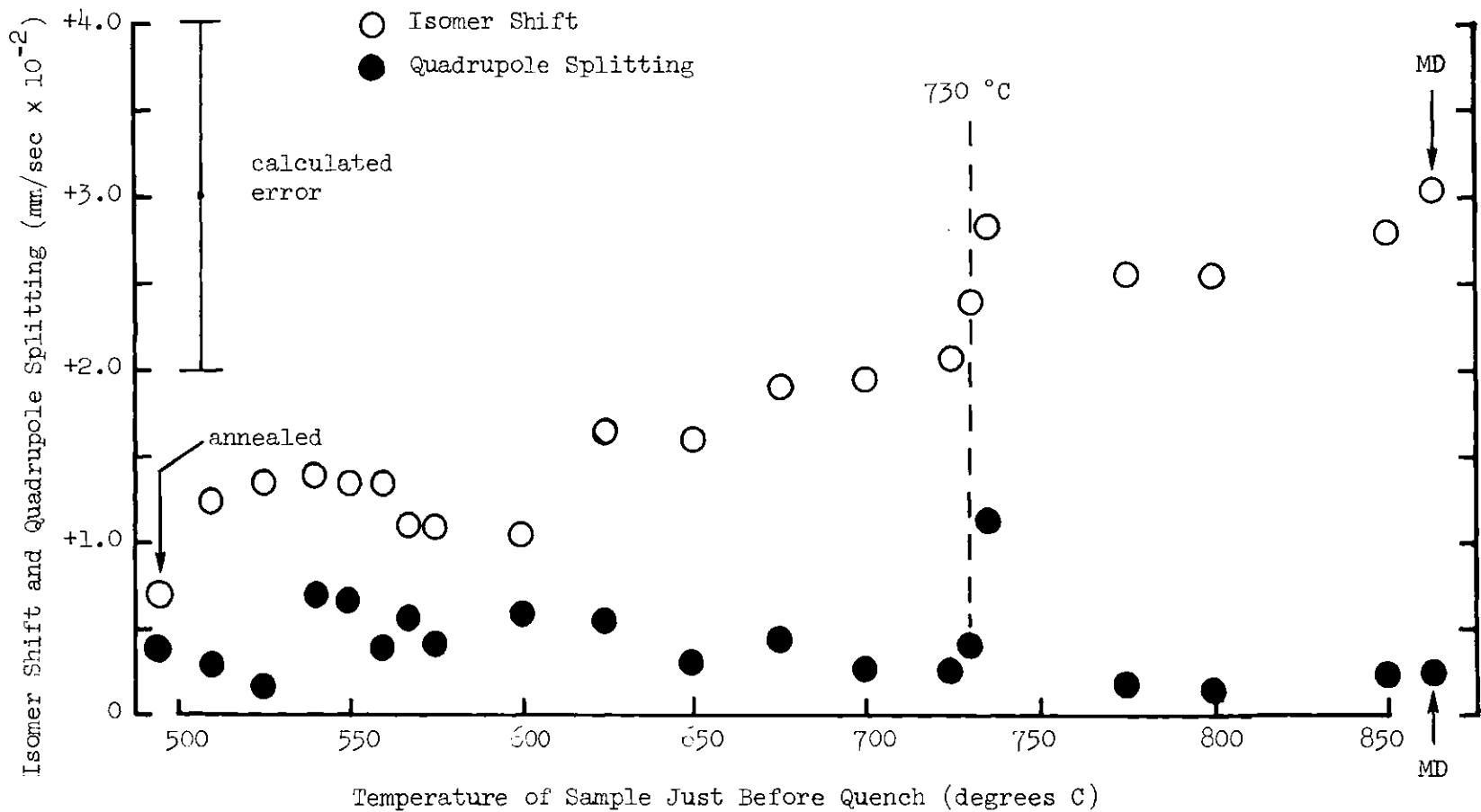
Figure 22. Isomer Shift and Quadrupole Splitting of Fe(50-50)Co versus the Temperature of the
Sample Just Before It Was Quenched. (Also shown are values for a sample ordered by
annealing and for a sample disordered by mechanical deformation (MD).)
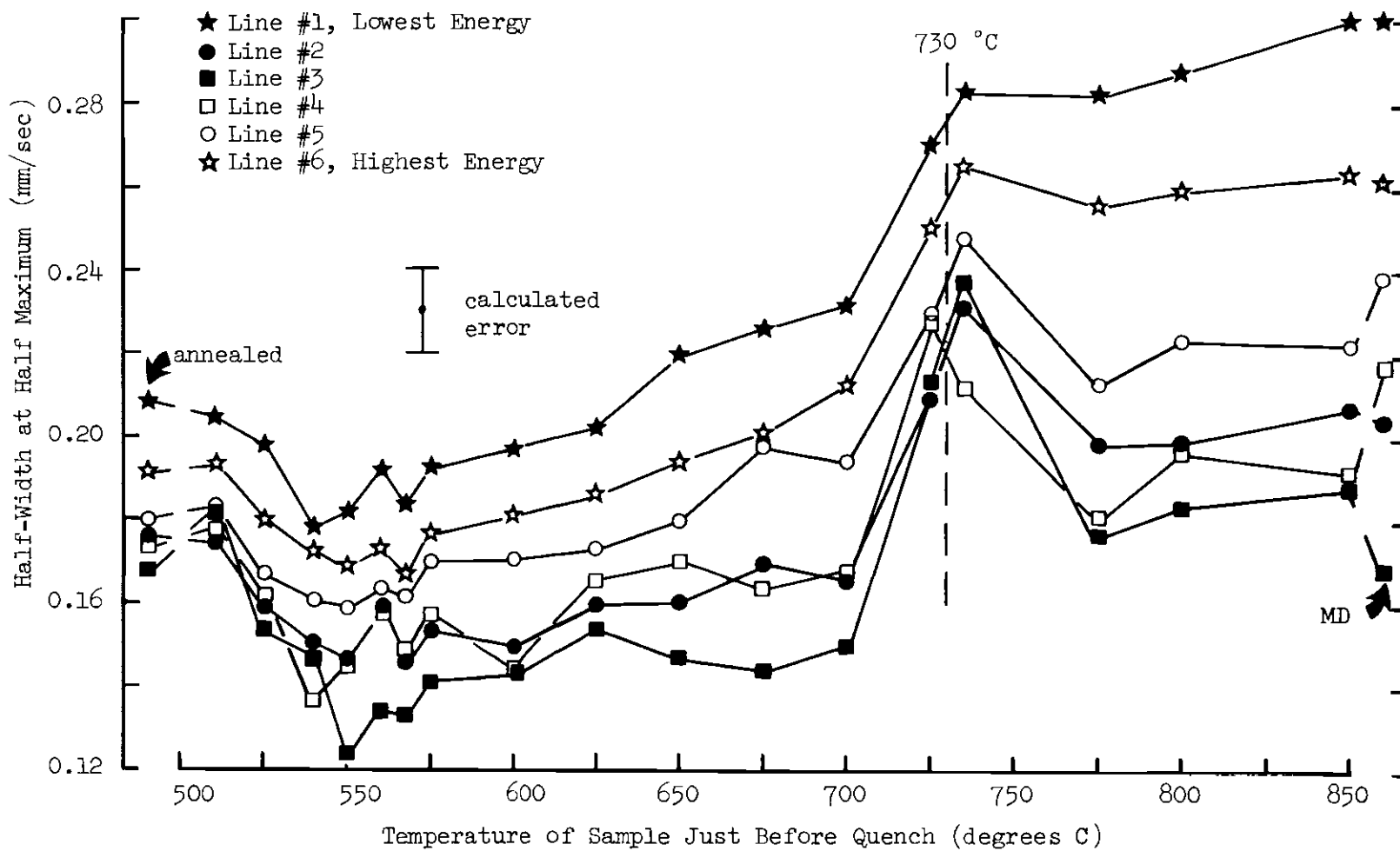
Figure 23. Line Widths of the Six Absorption Lines for Fe(50-50)Co versus the Temperature of the Sample Just Before It Was Quenched. (Also shown are values for a sample ordered by annealing and for a sample disordered by mechanical deformation (MD).)

quench temperature. Again, the temperature dependence is similar
to that of H_e and the isomer shift, with the widths being larger for
the absorption lines of the disordered samples than for those of the
more ordered samples. From the set of six curves shown in the
figure, it is seen that there was some small but detectable asymmetry
in line width for each spectrum, although no such effects were
observed in pure iron samples and even though the error limits were
relatively large. Nevertheless, the overall dependence of the HWHM
of each line on order-disorder is not affected and the implications
concerning local interactions discussed above are not changed. The
origin of the asymmetrical line broadening is unclear and could result
only from a complex combination of the interactions known to be at work
in the alloys.

CHAPTER IV

CONCLUSIONS

Mössbauer spectroscopy has been used to gain detailed
information about the effects of atomic configurational changes
in the 25-75 percent composition region of the iron-cobalt alloy
system. The results indicate that there are competing contributions
to the hyperfine interactions and that some of these contributions
are dependent on local atomic environment. Also indicated is a
spin polarization of the conduction electrons which is positive in
sign. In addition, the possibility has been established for using
the Mössbauer effect to determine the temperature dependence of the
short range order parameter.

It is hoped that the highly precise measurements of this
research will be of benefit in establishing the theoretical description
of transition metal alloys on a more quantitative basis. Additional
information which should be of help in this effort could be obtained
by similar detailed Mössbauer studies on alloys of iron with other
transition metals such as manganese, vanadium, and chromium. The
correlation of such studies with neutron diffraction measurements
should assist in gaining further insight into the usefulness of
Mössbauer spectroscopy to characterize the short range order of alloys.

APPENDIX

TABULATION OF MÖSSBAUER DATA

The Appendix consists of six tables which give a complete tabulation of the Mossbauer data. The following abbreviations are used: MD for mechanical deformation and FQ for fast quench from above the ordering temperature.

Table 1. Effective Magnetic Field versus Composition

Composition (percent Cobalt)	Effective Magnetic Field (kOe)		
	Ordered by Annealing	Disordered by FQ	Disordered by MD
25	-365.5 ± 0.4	-366.9 ± 0.3	-365.5 ± 0.6
40	-353.0 ± 0.3	-358.1 ± 0.3	-358.5 ± 0.3
50	-340.0 ± 0.3	-348.9 ± 0.3	-341.3 ± 0.3
60	-338.0 ± 0.3	-342.0 ± 0.4	-341.3 ± 0.3
75	-331.4 ± 0.5	-330.4 ± 0.6	-330.3 ± 0.7

Table 2. Isomer Shift and Quadrupole Splitting versus Composition.

Composition (percent Cobalt)	Isomer Shift (mm/sec x 10^{-2})			Quadrupole Splitting (mm/sec x 10^{-2})		
	Ordered by Annealing	Disordered by FQ	Disordered by MD	Ordered by Annealing	Disordered by FQ	Disordered by MD
25	+3.4 ± 1.5	+3.7 ± 1.5	+3.4 ± 1.0	0.3 ± 1.5	0.0 ± 1.5	0.3 ± 1.0
40	+2.0 ± 1.0	+3.2 ± 1.0	+3.8 ± 1.2	0.6 ± 1.0	0.0 ± 1.0	0.2 ± 1.2
50	+1.1 ± 1.0	+2.7 ± 1.0	+3.0 ± 1.2	0.4 ± 1.0	0.1 ± 1.0	0.3 ± 1.2
60	+1.0 ± 1.0	+2.2 ± 1.2	+2.8 ± 1.5	0.5 ± 1.0	0.1 ± 1.2	0.4 ± 1.5
75	+1.8 ± 2.0	+1.8 ± 3.0	+2.4 ± 2.5	1.8 ± 2.0	0.2 ± 3.0	0.3 ± 2.5

Table 3. Half-Widths at Half Maximum for the Spectral Lines versus Composition.

Composition (percent Cobalt)	Sample	Half-Width at Half Maximum (mm/sec)					
		Line 1	Line 2	Line 3	Line 4	Line 5	Line 6
25	Ordered by Annealing	0.27 ± 0.01	0.23 ± 0.01	0.19 ± 0.02	0.17 ± 0.02	0.21 ± 0.01	0.27 ± 0.01
	Disordered by FQ	0.24 ± 0.01	0.19 ± 0.01	0.19 ± 0.02	0.15 ± 0.02	0.19 ± 0.02	0.26 ± 0.01
	Disordered by MD	0.24 ± 0.01	0.21 ± 0.01	0.18 ± 0.02	0.18 ± 0.02	0.19 ± 0.01	0.28 ± 0.01
40	Ordered by Annealing	0.22 ± 0.01	0.20 ± 0.01	0.18 ± 0.02	0.16 ± 0.02	0.17 ± 0.01	0.24 ± 0.01
	Disordered by FQ	0.26 ± 0.01	0.21 ± 0.01	0.17 ± 0.02	0.16 ± 0.02	0.20 ± 0.01	0.29 ± 0.01
	Disordered by MD	0.28 ± 0.01	0.22 ± 0.01	0.18 ± 0.02	0.17 ± 0.02	0.21 ± 0.01	0.31 ± 0.01
50	Ordered by Annealing	0.19 ± 0.01	0.18 ± 0.01	0.17 ± 0.01	0.17 ± 0.01	0.18 ± 0.01	0.21 ± 0.01
	Disordered by FQ	0.26 ± 0.01	0.22 ± 0.01	0.20 ± 0.01	0.18 ± 0.01	0.20 ± 0.01	0.29 ± 0.01
	Disordered by MD	0.26 ± 0.01	0.24 ± 0.01	0.22 ± 0.01	0.17 ± 0.01	0.20 ± 0.01	0.30 ± 0.01
60	Ordered by Annealing	0.18 ± 0.01	0.18 ± 0.01	0.13 ± 0.01	0.15 ± 0.02	0.17 ± 0.01	0.21 ± 0.01
	Disordered by FQ	0.23 ± 0.01	0.22 ± 0.01	0.18 ± 0.02	0.16 ± 0.02	0.18 ± 0.01	0.27 ± 0.01
	Disordered by MD	0.27 ± 0.01	0.24 ± 0.01	0.17 ± 0.02	0.17 ± 0.02	0.20 ± 0.01	0.31 ± 0.01
75	Ordered by Annealing	0.19 ± 0.02	0.17 ± 0.02	0.15 ± 0.03	0.16 ± 0.03	0.17 ± 0.02	0.24 ± 0.02
	Disordered by FQ	0.24 ± 0.02	0.19 ± 0.02	0.13 ± 0.03	0.11 ± 0.03	0.16 ± 0.02	0.26 ± 0.02
	Disordered by MD	0.21 ± 0.02	0.21 ± 0.02	0.17 ± 0.03	0.18 ± 0.03	0.20 ± 0.02	0.25 ± 0.02

Table 4. Effective Magnetic Field, Isomer Shift, and Quadrupole
Splitting for Fe(50-50)Co Samples versus Quench Temperature.

Sample*	Effective Magnetic Field (kOe)	Isomer Shift (mm/sec x 10^{-2})	Quadrupole Splitting (mm/sec x 10^{-2})
Annealed	-339.7 ± 0.2	+0.7 ± 1.0	0.4 ± 1.0
510	-339.8 ± 0.2	+1.3 ± 1.0	0.3 ± 1.0
525	-339.5 ± 0.2	+1.4 ± 1.0	0.2 ± 1.0
540	-339.6 ± 0.5	+1.4 ± 1.0	0.7 ± 1.0
550	-339.8 ± 0.2	+1.4 ± 1.0	0.7 ± 1.0
560	-340.4 ± 0.3	+1.3 ± 1.0	0.4 ± 1.0
567	-340.4 ± 0.3	+1.1 ± 1.0	0.6 ± 1.0
575	-341.1 ± 0.3	+1.1 ± 1.0	0.4 ± 1.0
600	-341.4 ± 0.4	+1.1 ± 1.0	0.6 ± 1.0
625	-342.6 ± 0.3	+1.6 ± 1.0	0.6 ± 1.0
650	-343.6 ± 0.6	+1.6 ± 1.0	0.3 ± 1.0
675	-344.1 ± 0.4	+1.9 ± 1.0	0.5 ± 1.0
700	-345.4 ± 0.2	+2.0 ± 1.0	0.3 ± 1.0
725	-346.8 ± 0.2	+2.1 ± 1.0	0.3 ± 1.0
735	-348.9 ± 0.3	+2.9 ± 1.0	1.1 ± 1.0
775	-349.0 ± 0.3	+2.7 ± 1.0	0.2 ± 1.0
800	-348.9 ± 0.3	+2.6 ± 1.0	0.1 ± 1.0
850	-348.9 ± 0.3	+2.8 ± 1.2	0.2 ± 1.2
MD	-349.3 ± 0.4	+3.0 ± 1.1	0.3 ± 1.1

*Temperatures given are the quench temperatures, in degrees C.

Table 5. Half-Widths at Half Maximum for Fe(50-50)Co Spectral
          Lines versus Quench Temperature.

Sample[*]	Half-Width at Half Maximum (mm/sec)[**]					
	Line 1	Line 2	Line 3	Line 4	Line 5	Line 6
Annealed	0.21	0.18	0.17	0.17	0.19	0.19
510	0.21	0.18	0.18	0.18	0.18	0.19
525	0.20	0.16	0.15	0.16	0.17	0.18
540	0.17	0.16	0.14	0.15	0.15	0.18
550	0.17	0.16	0.15	0.12	0.14	0.18
560	0.17	0.16	0.16	0.13	0.16	0.19
567	0.17	0.16	0.15	0.13	0.15	0.18
575	0.18	0.17	0.16	0.14	0.15	0.19
600	0.18	0.17	0.14	0.14	0.15	0.20
625	0.19	0.17	0.17	0.15	0.16	0.20
650	0.19	0.18	0.15	0.15	0.16	0.22
675	0.20	0.20	0.16	0.14	0.17	0.23
700	0.21	0.20	0.17	0.15	0.17	0.23
725	0.25	0.23	0.23	0.21	0.21	0.27
735	0.27	0.25	0.21	0.23	0.23	0.28
775	0.26	0.21	0.18	0.20	0.20	0.28
800	0.26	0.22	0.20	0.20	0.20	0.29
850	0.26	0.22	0.19	0.21	0.21	0.30
MD	0.26	0.24	0.22	0.20	0.20	0.30

*Temperatures given are the quench temperatures, in degrees C.
**All errors are less than ± 0.01 mm/sec.

BIBLIOGRAPHY[*]

1. M. Hansen, <u>Constitution of Binary Alloys</u>, 2nd ed., McGraw-Hill, New York, 1958, p. 471.

    R. P. Elliot, <u>Constitution of Binary Alloys, First Supplement</u>, McGraw-Hill, New York, 1965, p. 319.

2. J. C. Slater, Journ. Appl. Phys. $\underline{8}$, 385 (1937).

3. L. Pauling, Phys. Rev. $\underline{54}$, 899 (1938).

4. J. Crangle, Article in <u>Electronic Structure and Alloy Chemistry of the Transition Elements</u>, P. A. Beck, ed., Interscience Publishers, New York, 1963, p. 51.

5. D. I. Bardos, Journ. Appl. Phys. $\underline{40}$, 1371 (1969).

6. M. F. Collins and J. B. Forsyth, Phil. Mag. $\underline{8}$, 401 (1963).

7. V. I. Goman'kov and A. A. Loshmanov, Bull. Ac. Sc. USSR Phys. $\underline{28}$, 357 (1964).

8. H. Asano, Y. Bando, N. Nakanishi, and S. Kachi, Trans. Japan. Inst. Metals $\underline{8}$, 180 (1967).

9. H. Masumoto, H. Saito, and M. Shinozaki, Sc. Rept. Research Insts. Tohoku Univ. $\underline{6}$, 523 (1954).

10. C. H. Cheng, C. T. Wei, and P. A. Beck, Phys. Rev. $\underline{120}$, 426 (1960).

11. F. E. Hoare, J. C. Matthews, and J. C. Walling, Proc. Roy. Soc. (London) $\underline{A216}$, 502 (1953).

12. F. E. Hoare, Article in <u>Electronic Structure and Alloy Chemistry of the Transition Elements</u>, P. A. Beck, ed., Interscience Publishers, New York, 1963, p. 29.

13. G. K. Wertheim, V. Jaccarino, J. H. Wernick, and N. D. E. Buchanan, Phys. Rev. Letters $\underline{12}$, 24 (1964).

14. M. Rubinstein, Phys. Rev. $\underline{172}$, 277 (1968).

---

[*] Abbreviations used herein follow the form of the American Institute of Physics <u>Style Manual</u>.

15. S. S. Hanna, J. Heberle, C. Littlejohn, G. J. Perlow, R. S. Preston, and D. H. Vincent, Phys. Rev. Letters 4, 177 (1960).

16. S. S. Hanna, J. Heberle, G. J. Perlow, R. S. Preston, and D. H. Vincent, Phys. Rev. Letters 4, 513 (1960).

17. J. I. Budnick, L. J. Bruner, R. J. Blume, and E. L. Boyd, Jr., Journ. Appl. Phys. 32, 102S (1961).

18. C. E. Johnson, M. S. Ridout, T. E. Cranshaw, and P. E. Madsen, Phys. Rev. Letters 6, 450 (1961).

19. C. E. Johnson, M. S. Ridout, and T. E. Cranshaw, Article in Second International Mössbauer Conference (1961), John Wiley, New York, 1961, p. 142.

20. C. E. Johnson, M. S. Ridout, and T. E. Cranshaw, Proc. Phys. Soc. 81, 1079 (1963).

21. B. deMayo, D. W. Forester, and S. Spooner, Bull. Am. Phys. Soc. 13, 1706 (1968), and 14, 99 (1969).

22. T. Muto and Y. Takagi, Sol. St. Phys. 1, 193 (1955).

23. L. Guttman, Sol. St. Phys. 3, 145 (1959).

24. V. I. Iveronova and A. A. Katsnel'son, Phys. Met. Metall. 24, 190 (1967).

25. N. S. Stoloff and R. G. Davies, Progress in Materials Science 13, 1 (1966).

26. W. L. Bragg and E. J. Williams, Proc. Roy. Soc. A 145, 699 (1934) and 151, 540 (1935).

27. J. M. Cowley, Phys. Rev. 77, 699 (1950) and 120, 1648 (1960).

28. H. A. Bethe, Proc. Phys. Soc. (London) 150, 231 (1935).

29. R. L. Mössbauer, Z. Phys. 151, 124 (1958), Naturwissenschaften 45, 538 (1958), and Z. Naturforsch, 14a, 211 (1958).

30. A. J. F. Boyle and H. E. Hall, Rept. Prog. Phys. 25, 441 (1962).

31. H. Frauenfelder, The Mössbauer Effect, W. A. Benjamin, Inc., New York, 1963.

32. G. K. Wertheim, The Mössbauer Effect. Principles and Applications, Academic Press, New York, 1964.

33. V. I. Gol'danskii and R. H. Herber, ed., Chemical Applications of Mössbauer Spectroscopy, Academic Press, New York, 1968.

34. A. H. Muir, K. J. Ando, and H. M. Coogan, Mössbauer Effect Data Index 1958-1965, Interscience Publishers, New York, 1966.

35. A. Abragam, The Principles of Nuclear Magnetism, Clarendon Press, Oxford, 1961, p. 172.

36. D. A. Goodings and V. Heine, Phys. Rev. Letters 5, 370 (1960).

37. D. N. Pipkorn, C. D. Edge, P. Debrunner, G. DePasquali, H. G. Drickamer, and H. Frauenfelder, Phys. Rev. 135, A1604 (1964).

38. R. E. Watson and A. J. Freeman, Phys. Rev. 123, 2027 (1961).

39. A. J. Freeman and R. E. Watson, Article in Magnetism, vol. IIA, G. T. Rado and H. Suhl, ed., Academic Press, New York, 1965, p. 167.

40. R. E. Watson and A. J. Freeman, Article in Hyperfine Interactions, A. J. Freeman and R. B. Frankel, ed., Academic Press, New York, 1967, p. 53.

41. R. E. Watson, Article in Hyperfine Interactions, A. J. Freeman and R. B. Frankel, ed., Academic Press, New York, 1967, p. 413.

42. C. Herring, Article in Magnetism, vol. IV, G. T. Rado and H. Suhl, ed., Academic Press, New York, 1966, 148.

43. H. Brooks, Article in Electronic Structure and Alloy Chemistry of the Transition Elements, P. A. Beck, ed., Interscience Publishers, New York, 1963, p. 3.

44. O. C. Kistner and A. W. Sunyar, Phys. Rev. Letters 4, 412 (1960).

45. L. R. Walker, G. K. Wertheim, and V. Jaccarino, Phys. Rev. Letters 6, 98 (1961).

46. J. J. Spijkerman, F. C. Reugg, and L. May, Article in Symposium on Mössbauer Effect Methodology, vol. II, I. J. Gruverman, ed., Plenum Press, New York, 1966, p. 85.

47. A. Heilmann and W. Zinn, Z. Metallkde, 58, 113 (1967).

48. P. G. Shewmon, Diffusion in Metals, McGraw-Hill, New York, 1963, passim.

49. N. L. Peterson, Sol. St. Phys. 22, 409 (1968).

50. P. A. Flinn and S. L. Ruby, Phys. Rev. 124, 34 (1961).

51. M. B. Stearns, Phys. Rev. 147, 439 (1966).

52. E. Daniel, Article in Hyperfine Interactions, A. J. Freeman
     and R. B. Frankel, ed., Academic Press, New York, 1967, p. 712.

53. C. G. Shull and Y. Yamada, Journ. Phys. Soc. (Japan) 17(B-111),
     1 (1962).

54. C. G. Shull, Article in Magnetic and Inelastic Scattering of
     Neutrons by Metals, T. J. Rowland and P. A. Beck, ed., Gordon
     and Breach, New York, 1968, p. 15.

55. C. G. Shull, Article in Electronic Structure and Alloy Chemistry
     of the Transition Elements, P. A. Beck, ed., Interscience
     Publishers, New York, 1963, p. 69.

56. P. E. Mijnarends and L. Hambro, Phys. Letters 10, 272 (1964).

57. D. H. Anderson, Sol. St. Comm. 4, 189 (1966).

58. P. C. Gehlen and J. B. Cohen, Phys. Rev. 139, A844 (1965).

59. B. G. Lyashenko, D. F. Litvin, I. M. Puzey, and J. G. Abov,
     Journ. Phys. Soc. (Japan) 17(B-111), 49 (1962).

VITA

Benjamin deMayo was born on August 4, 1940, in Atlanta, Georgia, where he attended primary and secondary schools. He received a B.S. in Physics from Emory University in 1962, where he was elected a member of Phi Beta Kappa, Sigma Pi Sigma, and Alpha Epsilon Upsilon. After receiving an M.S. in Physics from Yale University, he entered the Georgia Institute of Technology in 1965. He is a member of the American Physical Society.